View metadata, citation and similar papers at core.ac.uk

brought to you by CORE

provided by University of New Mexico

University of New Mexico
UNM Digital Repository

Optical Science and Engineering ETDs

Engineering ETDs

2-14-2014

The study of photo-thermal lensing system and its applications

XUERONG ZHANG

Follow this and additional works at: https://digitalrepository.unm.edu/ose_etds

Recommended Citation

ZHANG, XUERONG. "The study of photo-thermal lensing system and its applications." (2014). https://digitalrepository.unm.edu/ose_etds/50

This Thesis is brought to you for free and open access by the Engineering ETDs at UNM Digital Repository. It has been accepted for inclusion in Optical Science and Engineering ETDs by an authorized administrator of UNM Digital Repository. For more information, please contact disc@unm.edu.

Candidate

Department

This thesis is approved, and it is acceptable in quality and form for publication:

Approved by the Thesis Committee:

, Chairperson

The study of photo-thermal lensing system and its applications

by

Xuerong Zhang

B.S.,China Jiliang University, 2009

THESIS

Submitted in Partial Fulfillment of the

Requirements for the Degree of

Master of Science

Optical Science and Engineering

The University of New Mexico

Albuquerque, New Mexico

December, 2013

©2013, Xuerong Zhang

Dedication

To my parents, My friends, for their support and encouragement.

Acknowledgments

This work is supported by JTO/ARO grant W911NF-11-1-007. There are a couple of people I wish to thank for their valuable contributions to this thesis. First of all, I would like to thank my advisor, professor Wolfgang Rudolph for his support and steady supply of good ideas over the years. I also would like to thank Dr.Luke Emmert for his valuable assistance in the design and operation of these experiments. Without their physical insight and expertise in the field this work would not have been possible.

I would also like to thank a number of other people including Drs.Kai Starke and Detlev Ristau of Laser Zentrum Hannover for supplying the high-quality sputtered TiO_2 films, Dr.Dinesh Patel and Professor Carmen Menoni at Colorado State University for the HfO_2 and Sc_2O_3films, Dr.Reed Weber for data acquisition LABVIEW program and Ms.Cristina Rodriguez for the third harmonic images. I would also like to thank my friends who worked with me on this and other projects: (Jim)Zhanliang Sun, Rhett Eller and Yejia Xu for both their technical assistance and for their friendly companionship. It has been a real pleasure working with them.

Finally, I wish to thank my family, especially for their love, support and encouragement.

The study of photo-thermal lensing system and its applications

by

Xuerong Zhang

B.S.,China Jiliang University, 2009

M.S., Optical Science and Engineering, University of New Mexico, 2013

Abstract

The high quality optical films in coatings with low absorption and good environmental stability are required for the development of high power lasers, because even slightest absorbing defects could lead to material's breakdown[1]. Thus, a non-destructive absorption measurement is required to measure the absorption of defects. Reflection-transmission method is the simplest measurement to measure the absorption of optical films. This indirect method is good for absorption values down to $\sim 0.1\%$. However, typical high quality optical coatings have absorption values measured in parts per million (ppm). In this thesis, the photo-thermal lens setup provides another way to measure the change in the sample related to heating with sensitivity up to 10^{-6}. This technique is a pump-probe technique which depends on a change in an optical property measured by a weak probe laser that results from heating by a strong pump. The photo-thermal setup is used to measure absorption with time resolution and identify defects in optical coatings.

Contents

List of Figures x

List of Tables xv

Glossary xvii

1 Introduction 1

1.1 Goals of Thesis 2

1.2 Outline of Thesis 3

2 Background 5

2.1 Absorption in Dielectrics 5

2.2 Absorption Measurements of Optical Coatings 8

2.2.1 Photo-thermal lensing technique 9

2.2.2 Photo-thermal deflection technique 10

2.3 The Absorption Coefficient 12

2.4 Summary 12

3 Photo-thermal absorption optimization 13

3.1 Experimental setup 13

3.2 Optimization parameters 15

3.3 Simulation and optimization 16

3.4 Noise analysis 21

3.5 Calibration 28

3.6 Optimized photo-thermal setup and detection limit 29

3.7 Longitudinal scans of samples 30

3.8 Summary 32

4 Time resolved absorption of thin films 33

4.1 Ion-beam sputtering TiO_2 time-resolved results 34

4.2 Absorption reduction by laser conditioning and thermal annealing . . 40

5 Combined absorption and scattering imaging 45

5.1 Sc_2O_3 scanning results 46

5.2 HfO_2 scanning results 48

6 Summary 50

Appendices 51

A Experimental Procedures **52**

B Lists of reference sample **55**

C How reproducible of the calibration sample experiment **57**

D Conversion of absorption coefficient from absorption **59**

E Absorption and scattering from dust **62**

F Substrate issue **66**

G Electron beam evaporation TiO_2 film results **69**

H Spike distributions of HfO_2 C and D **72**

I Model of photo-thermal signal **73**

J Overall absorption calculation for the sample with a single layer film **76**

References **79**

List of Figures

2.1 Transmission spectra of fused SiO_2 and borosilicate (BK7) windows. 6

2.2 Band model of absorption in dielectrics. Three absorption processes are shown: (a) single-photon band-to-band excitation; (b) multiphoton band-to-band excitation; and (c) excitation into empty defect states near the valence band edge. 7

2.3 Calculated temperature field for absorbing film on a non-absorbing fused silica substrate. (Film is on left side of graph.) film thickness = 100 nm; absorption= 10 ppm; pump power=1 W; pump Gaussian beam radius=15 microns. Peak temperature 220 mK. 9

2.4 Photo-thermal Common-path Interferometer setup[2] 10

2.5 (a),(b)The experimental setup for transverse and collinear Photo-thermal deflection spectroscopy(PDS) respectively [3] 11

3.1 Optical layout of photo-thermal setup 15

3.2 Schematic of photo-thermal lens 15

3.3 Comparison of photo-thermal signal between simulation and experiment vs. normalized d/z_p 17

3.4 The photo-thermal signal vs normalized iris size in near-field and far-field detection. The iris size is normalized to the probe size at the iris plane. 18

3.5 Photo-thermal signal vs probe focus to sample distance z' with detection distance 100 times larger than the probe Raleigh range. . . . 19

3.6 Contour plot of photo-thermal signal $p = \frac{\Delta s}{S}$ vs $z\prime$ and d. Both are normalized to z_p, the Rayleigh range of probe beam. 20

3.7 A Schematic of setup for measuring overall noise including power fluctuation and point stability from the laser source. 22

3.8 The noise equivalent signal caused by the pump laser at different chopper frequency (a) power fluctuation (b) both point stability and power fluctuation. 23

3.9 The noise equivalent signal caused by the probe laser source at different chopper frequency (a) power fluctuation (b) both probe point stability and power fluctuation. 23

3.10 The noise equivalent signal caused by probe and pump laser sources at different chopper frequency (a) power fluctuation (b) both point stability and power fluctuation. 24

3.11 The linear relationship between photo-thermal signal and input pump power 26

3.12 The photo-thermal signal of reference sample NDF03 vs. input pump power 29

3.13 Absorption of two HfO_2 samples with different thicknesses 30

3.14 The longitudinal scan of as-grown HfO_2 with 200nm film thickness on a quarter inch fused silica substrate 31

4.1 Third-harmonic microscope images(10μm by 10μm)of (a) IBS and (b) EBE TiO_2 films [4] 35

4.2 Time-resolved absorption of the IBS TiO_2 film for (a) pulsed illumination at (1) 57 kW/cm^2, (2) 110 kW/cm^2, and (3) 200 kW/cm^2 average irradiance; and (b) CW illumination 36

4.3 The initial absorption vs. the average irradiance for the IBS TiO_2 film under pulsed illumination. The absorption coefficient obtained with CW illumination is shown for comparison. 37

4.4 Simplified energy level scheme for TiO_2. (solid arrows = optical transitions; dashed arrows = relaxation processes.) Level A1, A2 is an existing trap state near VB and CB, respectively. B is a laser induced state. 38

4.5 Time-resolved absorption with relaxation for IBS film under pulsed illumination: (a) long-time scale; and (b) short-time scale 39

4.6 Absorption of as-grown and annealed HfO_2 samples respectively vs.time at a local spot under 532nm CW excitation with intensity $990kW/cm^2$. 41

4.7 The initial and final absorption of annealed and as-grown HfO_2 with different film thickness. The arrows indicate the changes. 42

4.8 The theoretical and experimental absorption results vs. film thickness 43

5.1 A layout of setup for simultaneously collecting scattering and absorption signals. 46

5.2 Left : Absorption image of Scandia with pump intensity 220kw/cm^2. Right : Scattering image of Scandia. The size of both images is 900μm $\times$ 136 μm and each pixel is 9μm $\times$9μm. 47

5.3 Three successive lateral line scans of Scandia film showing (a)absorption (b) scattering. 48

A.1 The schematic of aligning beams with the pinhole 53

C.1 Calibration factor of NDF03 reference sample measured on different days 57

D.1 Absorption vs.α for a given film index and thickness 60

E.1 The layout for the Nitrogen flow setup 62

E.2 (a)The lateral scan of a same line with low flow rate first and then high flow rate.(b)Lateral scan of a same line without flow rate and then with low flow rate. 63

E.3 (a)(b)Scanning lines of both absorption and scattering at two different places. 64

F.1 left: Time dependent absorption measurement layout. Right: The absorption of sample I vs time 67

F.2 The absorption of sample J vs time 67

F.3 left: Longitudinal scan measurement layout. Right: The absorption of sample J vs longitudinal position Z. 68

F.4 Lateral scan of cleaned sample I 68

G.1 Time-resolved absorption coefficient for the EBE film under (a) CW illumination at (1) 9.3 kW/cm^2, (2) 28 kW/cm^2, (3) 78 kW/cm^2, and (4) 141 kW/cm^2 irradiance; (b) pulsed illumination at (1) 9.3 kW/cm^2, (2) 25 kW/cm^2, (3) 87 kW/cm^2, and (4) 180 kW/cm^2 peak irradiance. 70

G.2 Initial absorption vs. irradiance of EBE film under CW illumination. 71

J.1 The schematic graph shows that the incident beam can be reflected , absorbed and transmitted by the test sample. 76

List of Tables

2.1 Bandgaps of some dielectric oxide films used for high reflection mirror coatings 6

3.1 Optimized parameters of photothermal setup 21

3.2 Chopper frequency with corresponding time constant 22

4.1 List of samples and corresponding labels in this thesis 41

4.2 Absorption coefficients of interface and volume, associated with corresponding absorption of sample C and A with different film thickness. 43

5.1 Scanning results for sample D(annealed) and C(as-grown) 49

B.1 Calibration samples on different substrate with 532 nm 56

B.2 Calibration sample AlO_x on fused silica under CW and pulsed excitations round 800 nm 56

E.1 Mean absorption and standard deviation measured at the same spot with different flow rates 63

F.1 The fused silica from different vendors 66

H.1 Scanning results for annealed and as-grown HfO_2 with 85 nm thickness 72

Glossary

Q	calibration correction factor
CB	conduction band
VB	valence band
SNR	signal noise ratio
APD	avalanche photo diode
p	photo-thermal signal
SNR	signal to noise ratio
CW	continuous wavelength
fs	femtosecond
s	second
FP	Fabry-Perot
OD	optical density
A	absorption
α	absorption coefficient

Glossary

nm	nano-meter
l	thickness of the thin film
n	refractive index of the thin film
φ	phase shift
ρ	density
C_ρ	heat capacity
Δ s	voltage change of detected probe beam
S	voltage of detected probe beam
G	rate of heat generated in the volume
N	number of detected photons
θ	phase difference between reference input and signal in the Lock in amplifier
m	beam size ratio between probe and pump beam at test sample plane
d	detection distance
$z\prime$	probe focus-to sample distance
z_p	probe laser confocal parameter
ϕ	on-axis phase shift
k	probe-laser wave vector
w_p	Gaussian beam-waist radius of probe at which the intensity drop to $\frac{1}{e^2}$ of their axis value

Glossary

w_0	Gaussian beam-waist radius of pump at which the intensity drop to $\frac{1}{e^2}$ of their axis value
P_e	averaged pump power incident on the test sample
P_p	averaged probe power incident on the test sample
CW	continuous wave
ν	chopper frequency
t_l	lock-in time constant
EBE TiO_2	TiO_2 thin film grown by electron beam evaporation technique
IBS TiO_2	TiO_2 thin film grown by ion beam sputtering technique
CB	conduction band
VB	valence band
U	pulse energy

Chapter 1

Introduction

The recent advances in optical coating manufacturing, such as laser conditioning[5] for specific materials and sophisticated vacuum deposition technologies[6], have facilitated a considerable increase in the laser induced damage threshold of optical components. However, in high power laser applications, such as micro-machining, surface cleaning, or nuclear fusion[7][8][9], even the slightest defect could lead to the material's breakdown. Therefore, it is important and necessary to develop an accurate tool as precursor centers of laser-induced damage to help us in the localization, detection, and identification of defects and would permit feedback of the production technology of microcomponents and substrates[1]. For past 20 years, the optical single-particle detection based on fluorescence has become an effective tool in molecular biology and materials science because of the low background of this technique [10]. Still, this technique has its inherent shortcoming that it could not be adopted in several applications. Indeed, the fluorescence of the defects in thin film coatings is extremely weak, almost all the absorbed energy is converted into heat[11]. The detection of nanometer-sized inclusions embedded in thin films or substrates is turned out to be difficult with using only the classical optical technique (e.g., Bright-field , dark-field or Nomarski microscope)[12].Previous attempts to non-

destructively identify fluence-limiting defects by various microscopy techniques including Scanning Electron Microscopy(SEM) and Atomic Force Microscopy (AFM) have only identified critical geometrical features or scatter characteristics of coatings defects and laser damage threshold[13, 14, 15]. However, these instruments give no insight into seed stoichiometry or absorption[5]. Thus, with a different way of creating contrast, photo-thermal microscopes, including Photo-thermal common path interferometry[2], photo-thermal deflection microscope [3]and photo-thermal lens geometry[16], present effective methods to detect the absorption defects in thin films with high sensitivity.

The photo-thermal effect was first demonstrated in the nineteenth century, but this technique was not utilized for characterizing materials until 1970s. Then it is widely used in physics, analytical chemistry and medicine[17]. Photo-thermal microscope is a technique in which a heating beam is absorbed by a species to be detected, causing heat flow and a local change of refractive index. The propagation of a second beam, the probe, would be modulated by the heated area. These changes produce observed signals[18]. The photo-thermal signal is free from background and not sensitive to weak scattering since it only arises from absorbing centers that dissipate heat.

1.1 Goals of Thesis

1. To optimize the photo-thermal test instrument to obtain a ppm sensitivity and combine with spatial resolution to obtain distribution maps of absorbing sites. Thus we can investigate properties of the absorbing defects and distribution of those defects.

2. To apply this photo-thermal setup to get time resolution of optical materials such as, TiO_2 and HfO_2. The observation can explain the difference between the

multi-pulse laser-induced damage threshold and the fundamental value measured by single-pulse testing.

3. To obtain the correlation between absorbing and scattering signals to identify different kinds of defects.

1.2 Outline of Thesis

In Chapter 2 the origin of absorption in optical coatings is discussed. Also, the physical principles behind photo-thermal measurements of this absorption are reviewed.

In Chapter 3 the photo-thermal setup is presented. The optimization of the setup is demonstrated using modeling and experiments. The sources of noises are discussed. Finally the method of calibration is presented and the limit of detection identified.

In Chapter 4 the use of the photo-thermal setup to measure absorption with time resolution is demonstrated. Two examples are given. First, Laser-induced absorption in ion beam sputtered TiO_2 is studied. Second, the effect of laser conditioning and thermal annealing on the absorption of HfO_2 is presented.

In Chapter 5 the photo-thermal setup is applied to identify defects in optical coatings. Simultaneous mapping of absorption and scatter is presented that shows that localized absorption and/or scattering sites can be identified. The density of these sites is estimated.

In appendix, there are lists of things that we discussed in details including: (1) Experimental Procedures.(2) Lists of reference samples we have used throughout the thesis.(3) How reproducible of the calibration sample experiment.(4) Conversion of absorption coefficient from absorption.(5) Absorption and scattering from

dust.(6) Substrate issue.(7) Electron beam evaporation TiO_2 film under CW and pulsed beam.(8) Overall absorption calculation for a single layer film on top of fused silica substrate with given interface absorption coefficient α and volume absorption coefficient γ.

Chapter 2

Background

This chapter briefly presents a few key features of the photo-thermal technique used throughout this thesis. It begins with an introduction of optical absorption in dielectric materials. Then it is followed with a discussion in terms of thermal lens mechanism and different absorption detection geometries. Finally, the conversion from the measured absorption to absorption coefficient is discussed.

2.1 Absorption in Dielectrics

This thesis is concerned with the measurement of absorption in optical coatings. The most common materials for optical coatings are metal oxides because of their low absorption in the visible spectrum and good environmental stability. As an example, Fig. 2.1 shows the transmission spectra of fused silica and borosilicate (BK7) windows. The transmission is below 100% at all wavelengths due to Fresnel reflections at the surfaces. The BK7 window is transparent down to ∼300 nm. This absorption edge corresponds to point when the photon energy ($h\nu$) equals the material band gap energy (E_g). The band gap energies of some oxides commonly

used in optical coatings are listed in Table 2.1.

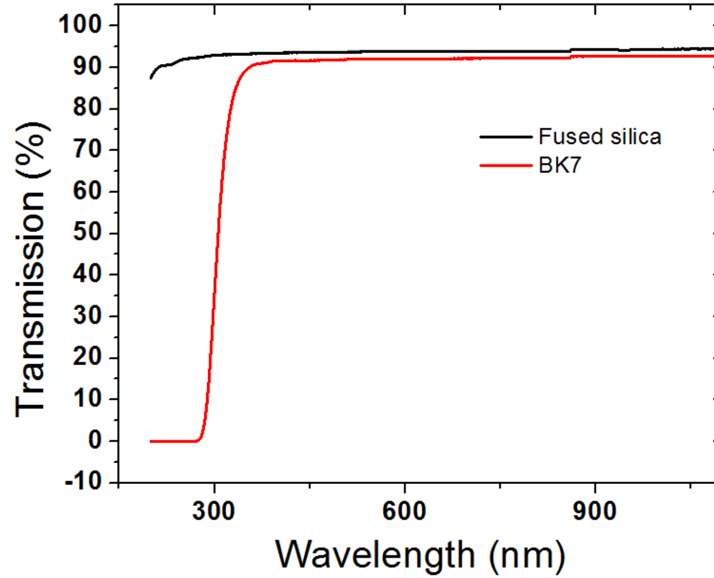

Figure 2.1: Transmission spectra of fused SiO_2 and borosilicate (BK7) windows.

Dielectric Oxide film	Bandgap[eV]
TiO_2	3.3[19]
HfO_2	5.1[19]
Al_2O_3	6.5[19]
SiO_2	8.3[19]
Sc_2O_3	5.7[20] ,6.3[20]

Table 2.1: Bandgaps of some dielectric oxide films used for high reflection mirror coatings

The general features of the transmission spectra can be described by an ideal dielectric (see Fig. 2.1). Absorption is due to excitation of an electron from a completely filled valence band to an empty conduction band. For linear absorption, this requires that the photon energy be greater than the band gap energy ($h\nu > E_g$, see Fig. 2.2(a)). For photon energies below the band gap, multiphoton absorption,

where 2 or more photons are absorbed while exciting the electron, is required (see Fig. 2.2(b)). Multiphoton absorption is important at the high intensities reached in pulsed laser systems.

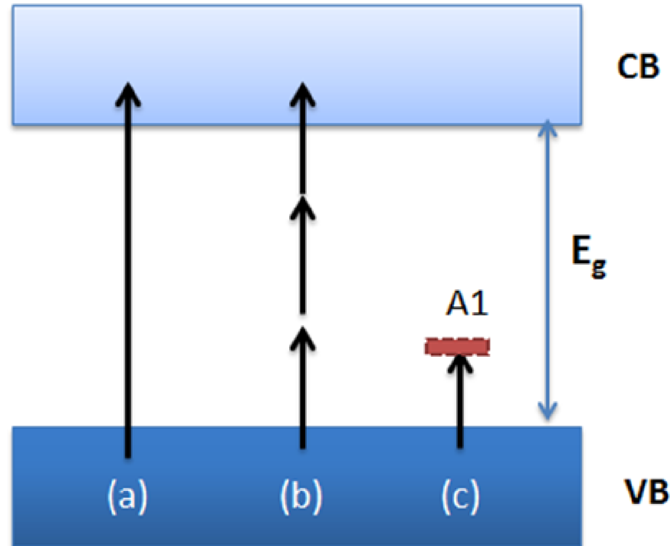

Figure 2.2: Band model of absorption in dielectrics. Three absorption processes are shown: (a) single-photon band-to-band excitation; (b) multiphoton band-to-band excitation; and (c) excitation into empty defect states near the valence band edge.

In real materials, linear absorption still occurs for photon energies well below the band gap due to defects such as interstitials and vacancies in the material which create states within the band gap. As an example Fig. 2.2(c) shows excitation into a state near the valence band. This is just one example of a defect state. Other states throughout the band gap are predicted from first-principles calculation[21]. Point defects (e.g. vacancies and interstitials) are inevitable even in single-crystals[22]. Optical coating processes produce films far from equilibrium and result in higher densities of defects than bulk materials. In addition, defects can be created and eliminated by laser illumination itself. Intrinsic and laser-induced defects have been used to explain the laser-induced damage behavior of dielectric films[23].

2.2 Absorption Measurements of Optical Coatings

The simplest technique to measure the absorption of an optical coating on a weakly absorbing substrate, is to measure the transmitted power P_T and the reflected power P_R. By energy conservation, the absorption A is given by

$$A = 1 - (P_T + P_R)/P_0$$

where P_0 is the incident power. (This assumes that the scattered power and absorption by the substrate are negligible.) This *indirect* method is good for absorption values down to ~0.1% and is limited by the accuracy of the power measurements.

Typical high quality optical coatings have absorption values measured in parts per million (ppm). The absorbed power can be measured *indirectly* through a change in the sample related to heating. One such method is laser calorimetry[24] which works by measuring the temperature change of the test sample using an attached temperature sensor. Photothermal techniques are all optical methods that depend on a change in an optical property measured by a weak probe laser that results from heating by a strong pump. They require that fluorescence can be neglected.

To illustrate the photo thermal method, Fig. 2.3 shows the temperature increase in the substrate caused by absorption in a thin film (100 nm thick and 10 ppm absorption) calculated by solving the heat diffusion equation[25]. The calculation parameters are described in the figure caption. In the figure, the film is too thin to resolve but the temperature change extends more than 10 microns into the substrate. This temperature field leads to a spatially varying change in the refractive index Δn through the thermo-optic coefficient dn/dT, i.e.

$$\Delta n = \frac{dn}{dT} \Delta T.$$

This spatially varying Δn produces a thermal lens which can be detected by its effect on the probe laser and related back to the absorption of the pump. There have been

many demonstrations of the photothermal effect for absorption measurements[2, 3, 26], but they can be split into two classes based on the geometry of their pump-probe setup: photothermal lens and photothermal deflection. These are discussed in the next sections.

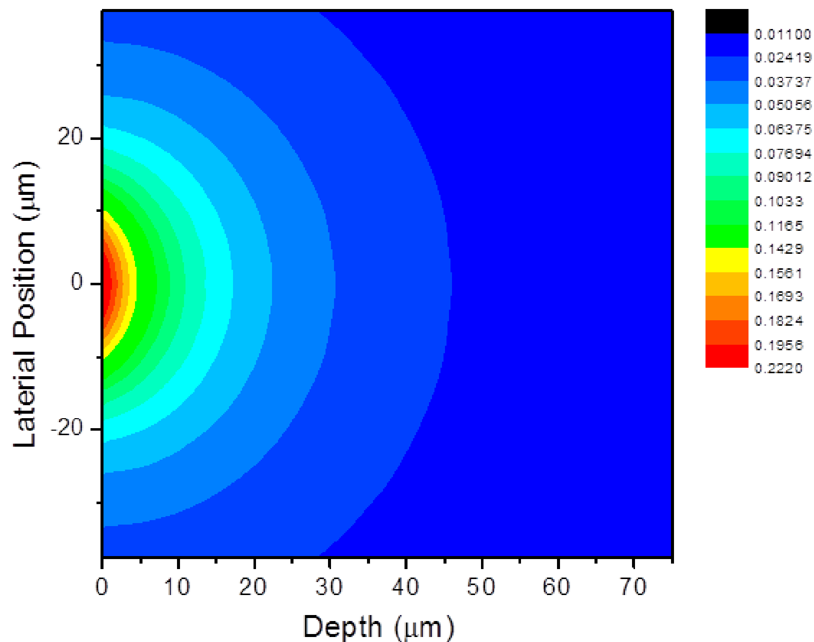

Figure 2.3: Calculated temperature field for absorbing film on a non-absorbing fused silica substrate. (Film is on left side of graph.) film thickness = 100 nm; absorption= 10 ppm; pump power=1 W; pump Gaussian beam radius=15 microns. Peak temperature 220 mK.

2.2.1 Photo-thermal lensing technique

The photo-thermal refraction technique (sometimes called PCI technique[2]) has become a effective tool to test various low absorption optical thin films and coatings. A schematic of the setup is shown in Figure. 2.4. And this is the geometry we use throughout this thesis.

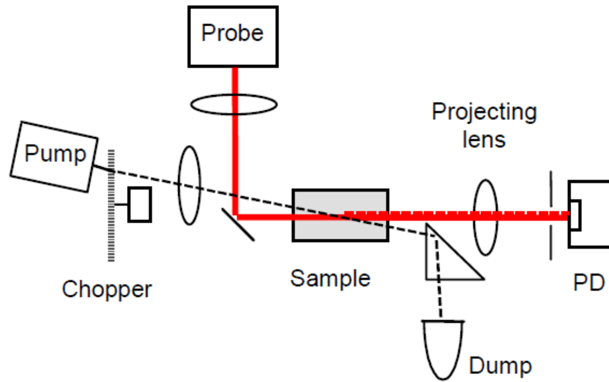

Figure 2.4: Photo-thermal Common-path Interferometer setup[2]

The technique is called a pump-probe technique in which a pump beam is focused into a material with a focusing lens, resulting in heating of the material. The heating causes the temperature rise and thus a local change in the refractive index of the material. Due to the spatial variation of the incident pump beam, a thermal lens is formed within the heat area. A second probe beam, with a waist larger than and power less than the heating probe beam, passes through the material. The probe beam is diverged by the thermal lens. An iris is used at the center of beam to acquire the intensity change due to thermal lens caused by pump beam.

2.2.2 Photo-thermal deflection technique

The photo-thermal deflection technique[3]distinguishes it from photo-thermal refractive technique in the way that the probe beam is deflected by the heated area which relates to the heating and the displacement of probe beam is detected by a position sensor.

The deflection technique is usually designed in two different geometries: transverse and collinear, see Figure. 2.5

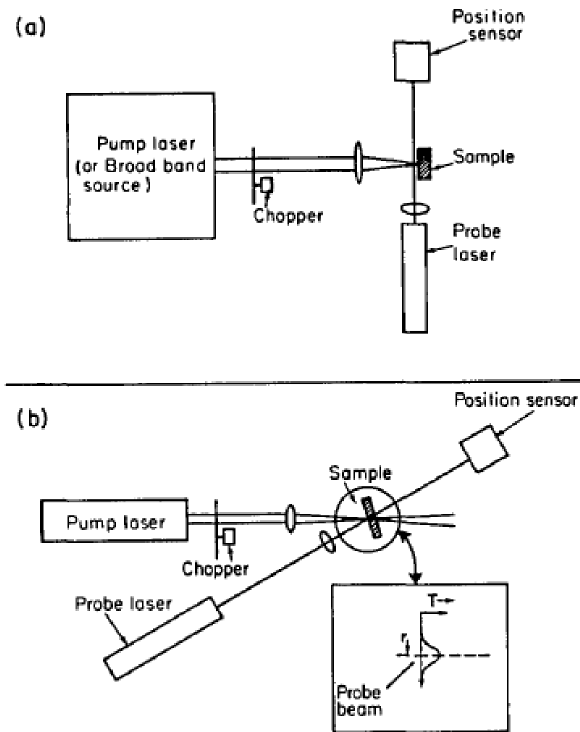

Figure 2.5: (a),(b)The experimental setup for transverse and collinear Photo-thermal deflection spectroscopy(PDS) respectively [3]

The collinear setup is difficult to align comparing with the transverse geometry, but it can perform 3-D depth profiling of absorption by moving the beam overlap region through the sample. The transverse PDS is good for measuring spectra of opaque samples or scattering samples. However, both techniques are limited by the point stability of probe laser in the case of low-frequency modulation. At high-frequency modulation, the limits are set by the stability of the probe laser and by the electronic noise of the position sensor.

2.3 The Absorption Coefficient

The measurements described in the previous section all measure the total absorption of the film, which depends on the thickness of the sample. When possible the absorption will be converted to the linear absorption coefficient, α, which can be related to defect absorption. This coefficient relates the laser intensity to the energy density absorbed, and can be related to the total absorption using the Beer-Lambert Law[27] which gives the intensity of a plane wave traveling through a uniformly absorbing material,

$$I(z) = I_0 \exp(-\alpha z)$$

For a slab of thickness d, the total absorption A is related to α by

$$\alpha = -\frac{1}{d} \ln(1 - A) \approx \frac{A}{d}$$

The latter is true for small absorptions (i.e. $A << 1$). In the case of thin films, the conversion from total absorption to absorption coefficient is complicated by multiple reflections off the air-film and film-substrate interfaces which create a Fabry-Perot effect[28]. Details of the conversion a given in Appendix D.

2.4 Summary

In optical coatings, absorption is possible for photon energies well below the band gap because of defects that result from the thin film deposition process. The absorption in high quality coatings approaches 1-10 ppm which cannot be detected by standard measurements with a spectrometer. Instead, techniques that are sensitive to the temperature changes caused by absorption are used. Photo-thermal methods are all optical pump-probe techniques that measure the local heating through the generation and detection of a thermal lens.

Chapter 3

Photo-thermal absorption optimization

In this chapter, photo-thermal setup with optimized parameters is sought to achieve high sensitivity as much as possible. In order to do that, photo-thermal signals should be improved by optimizing several parameters first. Secondly, sources of noise should be identified and minimized properly.

We start with introducing the layout of photo-thermal setup, and then make comparison between the simulation work[18] and our experimental results. Noise sources needed to be identified and proper ways to minimize noise needed to be found. Finally calibration is introduced in such as way that we can claim the sensitivity of current photo-thermal setup.

3.1 Experimental setup

The optical layout of the photo-thermal instrument used throughout the remainder of this thesis is shown in Fig. 3.1. A 532 nm frequency doubled Nd:Vanadate

laser(Coherent Verdi V-8) used as pump source is focused by a positive lens with 10 cm focal length. 632.8 nm He-Ne laser(AEROTECH) focused by a 4 cm lens is chosen to probe the thermal lens which is induced by pump beam. The test sample is located at the overlap of pump and probe beams. The alignment procedure is described in Appendix A. After test sample, the transmitted probe beam passing through an iris which samples just the center of the beam. After the iris, a lens images the probe beam into an avalanche photo-diode (Thorlabs APD110A2). A line filter(Thorlabs FL632.8-10) is used to block any laser sources except for the probe beam. A mechanical chopper(50% duty cycle) modulates pump beam and send reference signal to a DSP lock-in amplifier (Standard Research Systems,SRS830) which is used to measure the AC signal at the reference frequency. The DC level is measured using a digital oscilloscope (Tektronix, TDS210). The photo-thermal signal is defined as the relative probe intensity change which is given by

$$p = \frac{\Delta s}{S} \tag{3.1}$$

where Δs is AC signal measured by lock-in amplifier, S is the DC level measured by a digital oscilloscope.

Finally, an additional lens and photodetector shown in Fig.3.1 are used for collecting the scattered pump beam from sample surface. The scattered signal is measured with an analog Lock-in amplifier(Ithaco Dynatrac 391A) at the same frequency as the photo-thermal signal. The scatter measurements are discussed in Chapter 5.

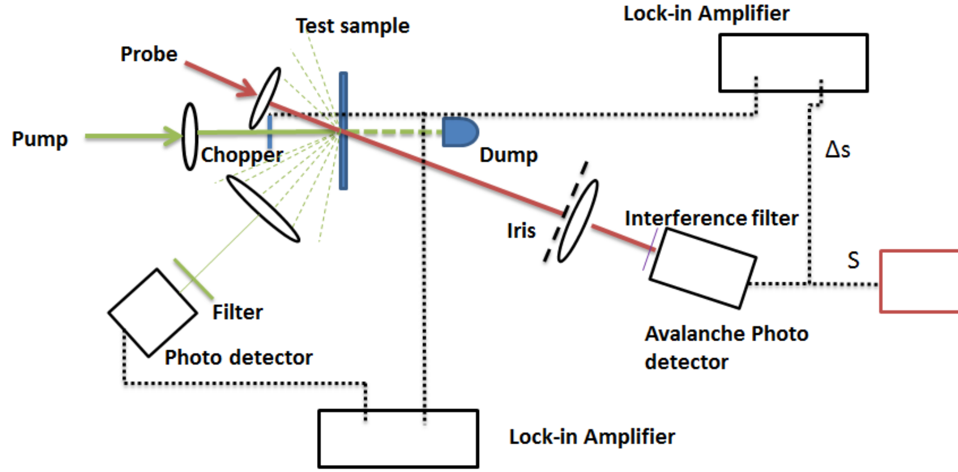

Figure 3.1: Optical layout of photo-thermal setup

3.2 Optimization parameters

The next section describes optimization of the photo-thermal signal through model and experiments. There are four parameters that are optimized and these are illustrated in Fig. 3.2.

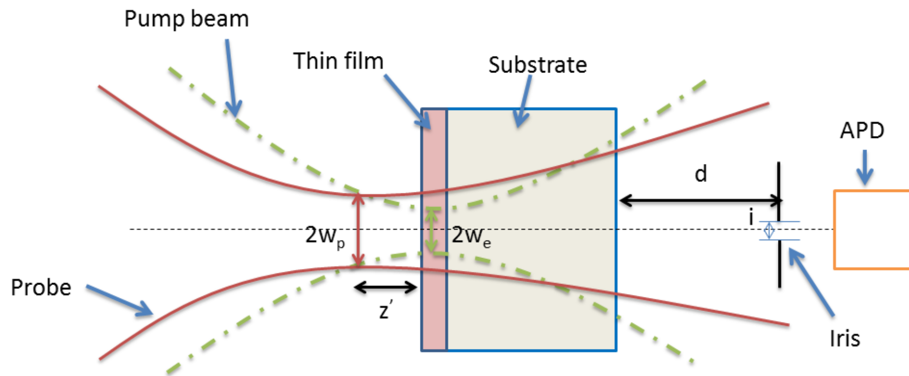

Figure 3.2: Schematic of photo-thermal lens

These parameters are distance from sample to the iris d, the size of the iris, the

distance between the probe focus and the sample surface z', and probe spot size w_p relative to the pump size w_e.

3.3 Simulation and optimization

The model we used for the photo-thermal was developed by Bialkowski[18]. The details of this model can be found in Appendix I. The final analytical expression for the photo-thermal signal estimated in Bialkowshi[18] with all the setup parameters

$$p \approx \frac{-8dkw^2(t)\varphi(t)(z_p^2 + z\prime^2 + dz\prime)}{k^2w^4(t)(z_p^2 + z\prime^2 + 2dz\prime + d^2) + 8kw^2(t)d^2z_p + 16d^2(z_p^2 + z\prime^2)}, \tag{3.2}$$

where $z\prime$ is the probe focus to sample distance, z_p is the Rayleigh range of probe laser, k wave-vector of the probe beam, d is the sample to iris distance, $\varphi(t)$ is the phase shift at the beam center caused by the thermal lens and $w(t)$ is the time dependent radius of the temperature change. The experimental result of intensity change p is shown in Eq 3.1. The following graphs shows how we optimized the parameters theoretically and experimentally.

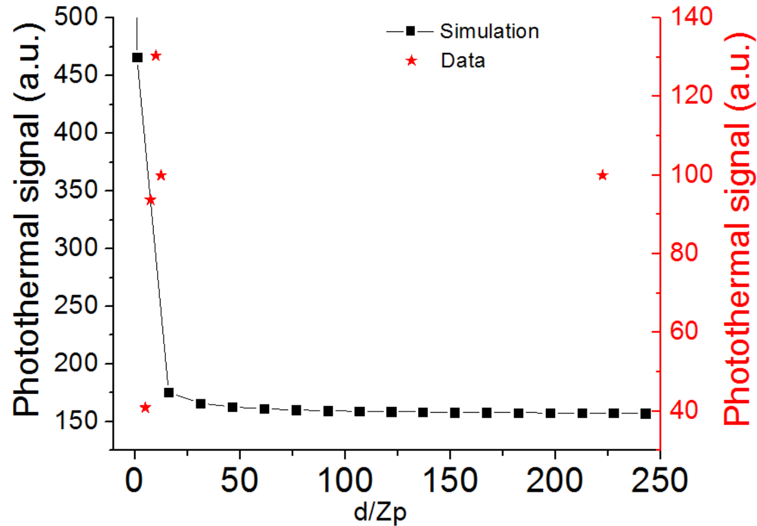

Figure 3.3: Comparison of photo-thermal signal between simulation and experiment vs. normalized d/z_p

Figure 3.3 shows a comparison of experimental and simulation results of the dependence on detection distance d. The black line in Figure. 3.3 shows the analytical result, indicating that the photo-thermal signal monotonically decreases with detection distance and the far-field signal is about 3 times less than that of the near-field signal. However, the red dots represent the real data measured with photo-thermal setup, where the photo-thermal signal increase first but then decrease with detection distance. And the far-field signal is about 30% less than the maximum one. The discrepancy of experiment and model results might caused by some assumptions in the model analysis. To achieve near-field detection, a projecting lens is needed to be used for imaging the point to the detector plane, which makes the alignment much more complicated. In our system, we choose far-field detection to make the alignment easier and it turns out that with current sensitivity we can measure the absorption of thin films discussed throughout this thesis. However, one could improve the sensitivity of current setup by 30% in the near-field detection based on what we have discussed above.

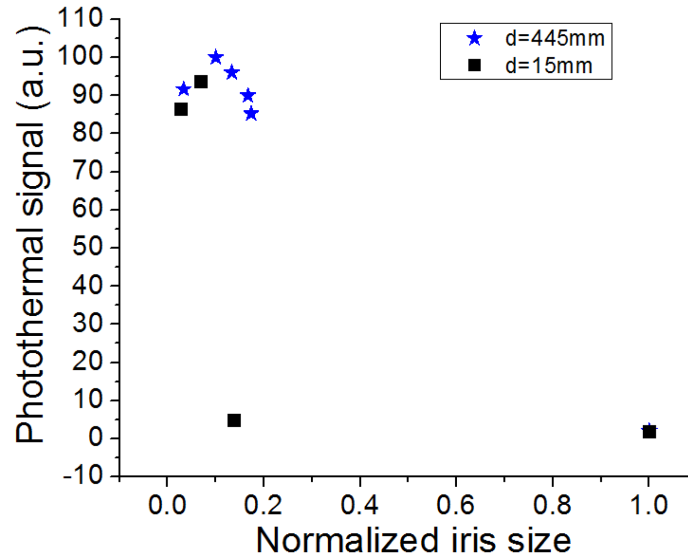

Figure 3.4: The photo-thermal signal vs normalized iris size in near-field and far-field detection. The iris size is normalized to the probe size at the iris plane.

Figure 3.4 shows the dependence of the photo-thermal signal on the iris size (normalized to the beam size on the iris plane) for two different values of the detection distance d. There is no simulation because of an approximation in the model derivation it does not include the effect of iris size. The photo-thermal signal is strongly dependent on the iris size. In Fig. 3.4, there are always optimized iris sizes both for near-field and far-field detection since too small iris size leads to weak probe intensity but no iris leads to no change in the probe intensity. The optimum iris size is about 1% of the beam size of the probe beam at iris plane no matter which detection scheme is chosen.

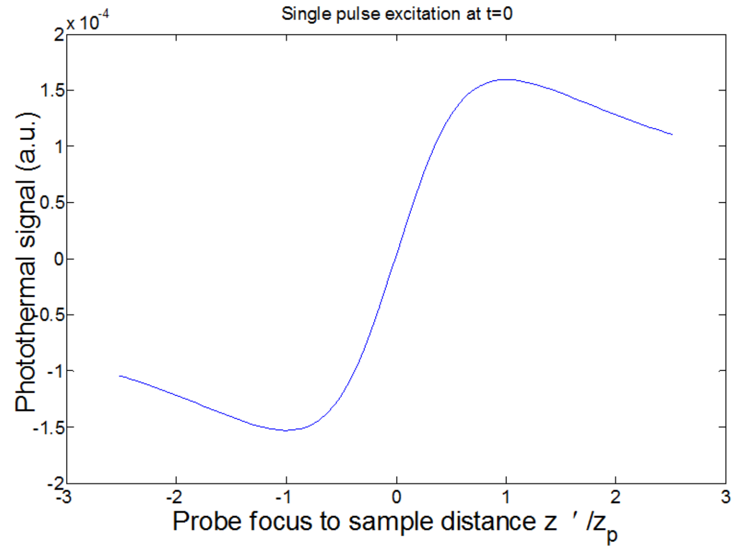

Figure 3.5: Photo-thermal signal vs probe focus to sample distance z' with detection distance 100 times larger than the probe Raleigh range.

Figure 3.5 shows the dependence of the photo-thermal signal on the focus to sample distance z' normalized to the Rayleigh range z_p. This calculation is for far field detection but the result is the same for near field.

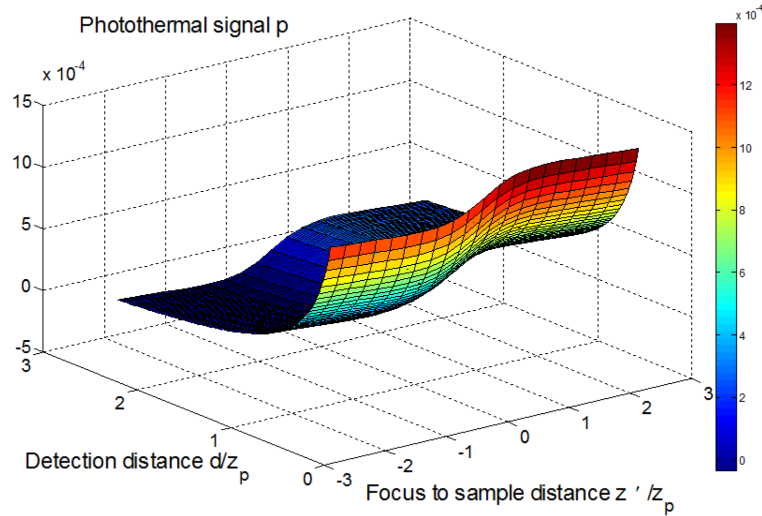

Figure 3.6: Contour plot of photo-thermal signal $p = \frac{\Delta s}{S}$ vs $z\prime$ and d. Both are normalized to z_p, the Rayleigh range of probe beam.

The resulting optimum focus position is $z' = \pm z_p$ shown in Fig. 3.5. However, we choose position value for z' since in Fig. 3.6 the overall maximum signal is obtained at the place where z'=z_p.

In summary, we have discussed optimization of the photo-thermal signal experimentally and theoretically. The photo-thermal signal is detected in the far-field scheme even though the signal is 30% higher in the near field detection scheme, because the alignment is easier. The iris size is always set to 1% of the beam size at the iris plane. The probe is focused to one Rayleigh range before the sample. The probe beam size is always chosen to be larger than that of the pump beam.

The optical layout of photo-thermal microscope was shown previously in Fig. 3.1. The following table 3.1 shows all the optimized parameters.

Symbol	Definition (Units)	Value
w_0	beam waist radius of pump (532 nm) μm	12.5
$w_{p,0}$	beam waist radius of probe (633 nm) μm	20
β	crossing angle between pump and probe (rad)	$\pi/6$
w_p	probe beam size at sample plane (μm)	45
z'	probe focus to sample distance (mm)	2
d	sample to iris distance (cm)	60
L	distance from lens4 to Photo detector(mm)	80
f_1	focal length of lens1 (mm)	100
f_2	focal length of lens2 (mm)	40
f_3	focal length of lens3 (mm)	140
f_4	focal length of lens4(mm)	50
P_e	averaged pump power incident on the test sample (W)	1∼6
P_p	averaged probe power incident on the test sample (mW)	< 1
ν	chopper frequency (Hz)	1100
t_l	Lock-in time constant (s)	0.3

Table 3.1: Optimized parameters of photothermal setup

3.4 Noise analysis

The detection limit is the smallest absorption which produces a signal that is larger than the noise. In the previous section, we have optimized the geometry of the photo-thermal setup to optimize the signal. In this section, we identify the noise sources in order to minimize them. The sources are the power fluctuations of pump and probe beams, point stability of pump and probe beams, and electronic noise from the detection system. These all have frequency dependence, so we will identify the frequency with lowest noise. To identify the noise sources, a schematic setup in Fig 3.7 works as a spectrum analyzer is used.

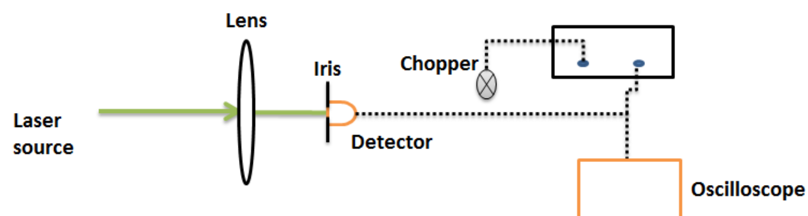

Figure 3.7: A Schematic of setup for measuring overall noise including power fluctuation and point stability from the laser source.

Iris is used for detecting both point stability and power fluctuation of laser source, and no iris for collecting power fluctuation from the laser source. The noise equivalent signal can be analyzed at different frequency by changing the chopper frequency. At each different reference frequency, a different lock-in time constant is chosen. The higher the reference frequency is, the smaller the time constant would be chosen. Since the $1/f$ noise fluctuation increases with reference frequency, a slower Lock-in time constant which reduces the measurement bandwidth is needed to obtain clean results. One can find the corresponding time constant and chopper frequency in table 3.2

chopper frequency [Hz]	time constant [s]
110	3
330	1
1100	0.3
3300	0.1

Table 3.2: Chopper frequency with corresponding time constant

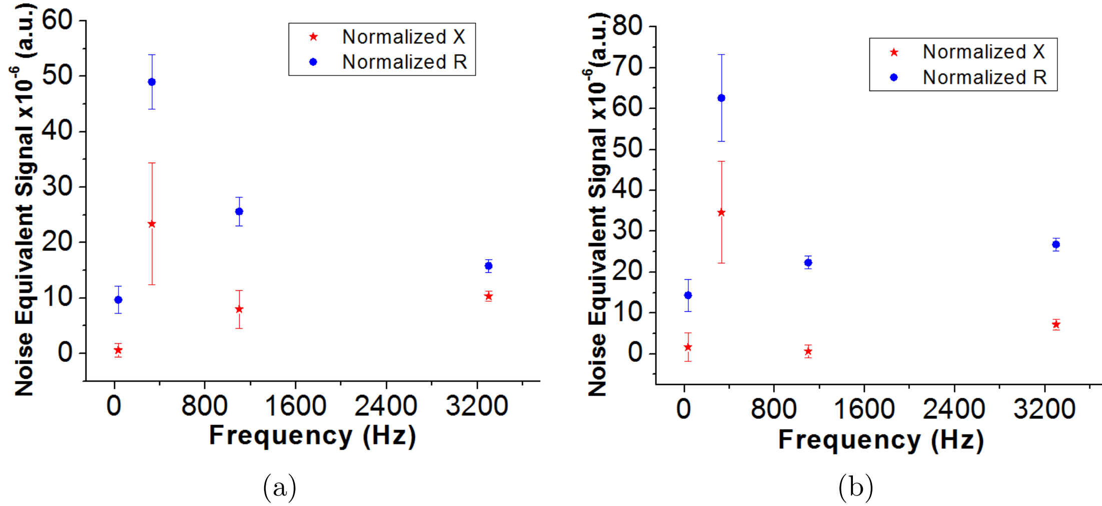

Figure 3.8: The noise equivalent signal caused by the pump laser at different chopper frequency (a) power fluctuation (b) both point stability and power fluctuation.

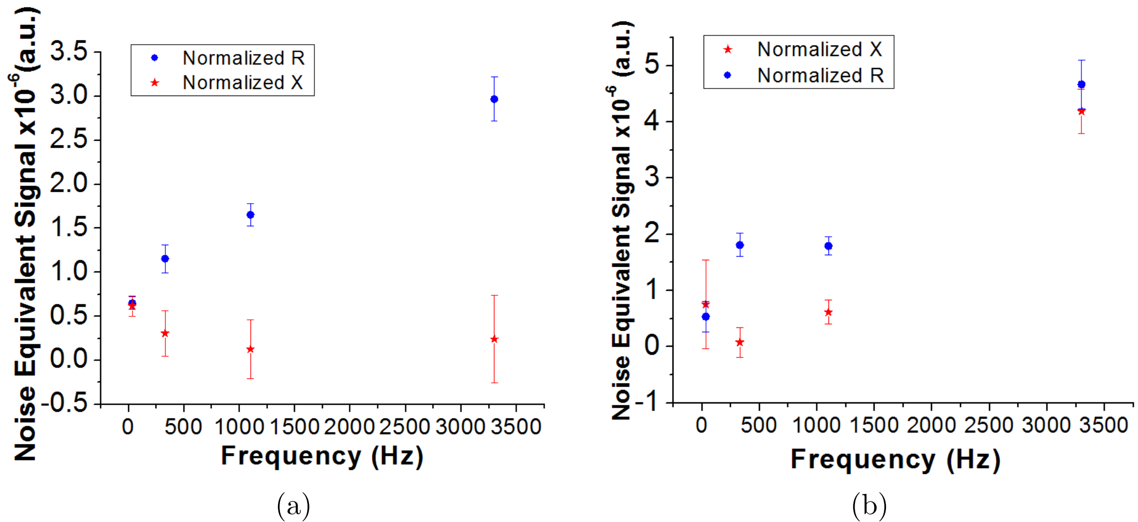

Figure 3.9: The noise equivalent signal caused by the probe laser source at different chopper frequency (a) power fluctuation (b) both probe point stability and power fluctuation.

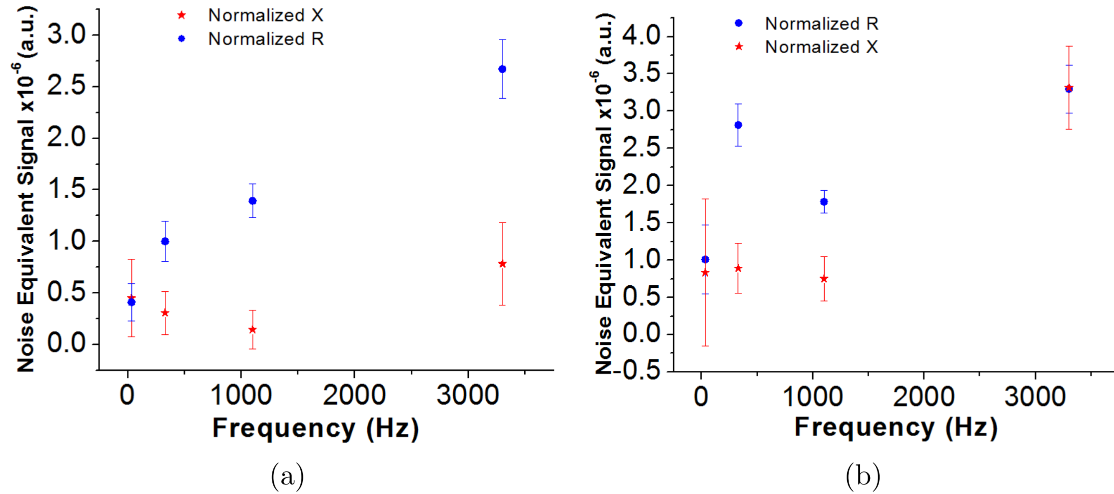

Figure 3.10: The noise equivalent signal caused by probe and pump laser sources at different chopper frequency (a) power fluctuation (b) both point stability and power fluctuation.

In Fig. 3.8, the magnitude of both pump power fluctuation and point stability are on the order of 10^{-5} and the noise levels in both cases are the maximum at 330Hz. In Fig. 3.9, the magnitude of both probe power fluctuation and point stability are on the order of 10^{-6} and noise levels in both cases are the maximum at 1.1kHz. However, in Fig. 3.10 the overall noise from both pump and probe power fluctuation and point stability are on the order of 10^{-6}, as the same order from the probe laser source only.

We identify that the noises are mainly from the probe laser source for reason that the pump makes much smaller effect on the final photo-thermal signal than that from the probe, although it has higher noise level. The pump beam affects the noise in an indirect way since any power fluctuations and point stability would give rise to uncertainties to the thermal lens which can be shown in the final probe signal change Δs. Δs is proportional to pump power and Δs fluctuation is also proportional to the pump power fluctuation and point stability based on the linear relationship shown in Fig. 3.11.

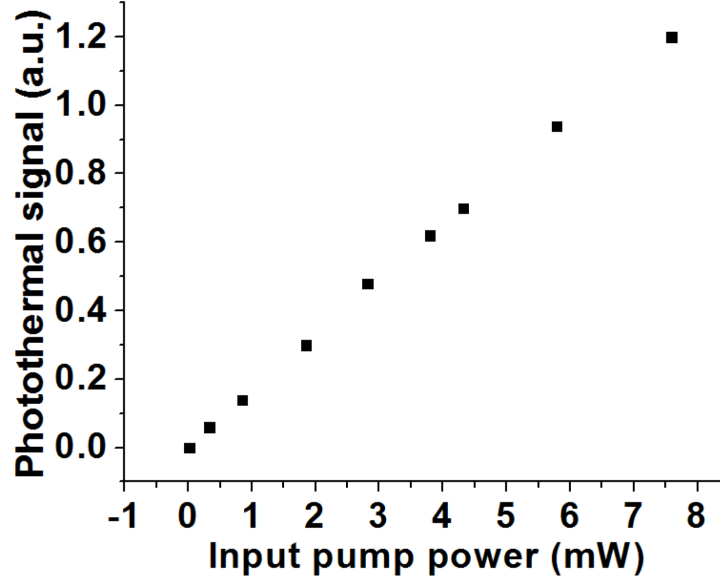

Figure 3.11: The linear relationship between photo-thermal signal and input pump power .

Then Δs_{noise} is related to Δs by

$$\Delta s_{noise} \approx 10^{-5}\ \Delta s, \tag{3.3}$$

where Δs_{noise} is Δs fluctuation and Δs is probe change caused by thermal lens. However, the probe laser source directly affect the photo-thermal signal because we detect the probe signal S and probe signal change Δs at the same time. The S fluctuation is also proportional to the probe power fluctuation and point stability. The relationship is expressed as,

$$S_{noise} \approx 10^{-6}\ S \tag{3.4}$$

where S_{noise} is S fluctuation that cause noise by the probe laser source, and S is the probe signal. For a typical dielectric thin film that we used in our thesis, the magnitude of photo-thermal is on the order of 10^{-5}, which means Δs is much smaller than S in such way,

$$\Delta s = 10^{-5}\ S. \tag{3.5}$$

We can compare the effect from pump(Δs_{noise}) with that from probe (S_{noise}) using the equations 3.3 3.4 3.5. We can get the relationship between the pump effect and probe effect,

$$\Delta s_{noise} = 10^{-10}\ S = 10^{-4}\ S_{noise}. \tag{3.6}$$

The effect from pump laser source is 10^4 smaller than that from probe laser source, and this is the reason why we can ignore the effect from pump source and identify the noise from probe laser only.

In phase component X and amplitude R of noise at different reference frequency are measured respectively. Based on those graphs, we can see that R is larger than X and there is relationship between X and R, such that

$$\mathrm{X} = \mathrm{R} * sin(\theta) \tag{3.7}$$

Where θ is the phase between the signal and the reference input.

All the magnitude of relative changes are on the order of 10^{-6}, but with the lowest level at 1.1 kHz chopper frequency. Therefore for all the signal and noise values we are going to discuss in the following chapters are in phase component X which have been measured at 1.1 kHz chopper frequency in order to achieve minimized noise level.

In addition to electronic noise, coherent radio frequency pickup adds a steady offset to the signal [29]. Any signal and reference cables and even power cord that plug into the lock in amplifier, picking up signals at reference frequency. This kind of effect would be dominant at frequencies above 5 MHz. Since current setup works at frequency below 1 MHz, we do not need to bother with this kind of noise source.

The last source of noise to be considered is optical noise. Scattered pump light at the reference frequency can easily overwhelm the measurement. However, in our system a line pass filter with center wavelength 633 nm and bandwidth 3 nm is used to block the pump beam produced no observable effect on the signal.

In this section, different kinds of noise have been discussed in details especially the laser noise. Compared to other noise sources, such as the shot noise level, the noise from the laser source itself dominates in this case. And the noise level is on the order of 10^{-6}, which limits the sensitivity of the setup. Therefore, in order to improve the sensitivity of the setup, laser source with low power fluctuation and high point stability would be considered.

3.5 Calibration

In order to convert the photo-thermal signal to absorption, we use a calibration sample which consists of a highly absorbing film on a substrate of the same material as the test sample. The absorption is calculated using

$$A = \frac{p}{p_r} \frac{P_r A_r}{P} \tag{3.8}$$

where A_r is the known absorption of the reference sample, A is the test sample absorption, P_r,P are the input pump power of reference and test samples. p_r,p are the photo-thermal signal of reference and test samples. The assumptions of this calibration procedure are that the thermal lens is in the substrate and does not depend on the film and the photo-thermal signal is linearly proportional to the pump power. The latter is shown in Fig. 3.12

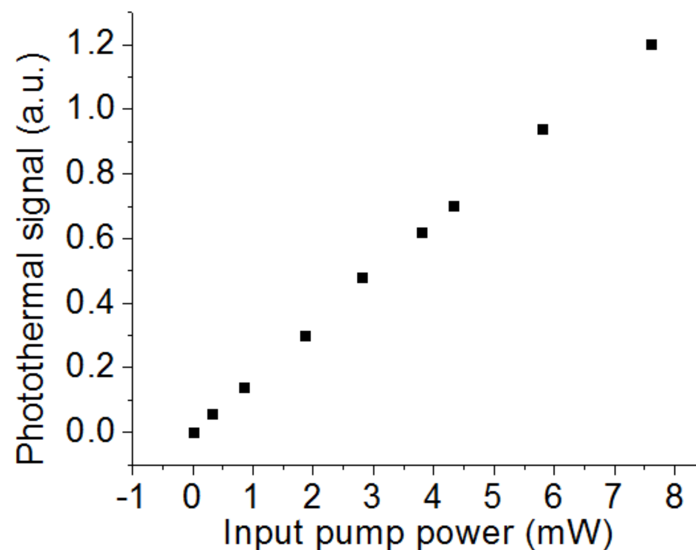

Figure 3.12: The photo-thermal signal of reference sample NDF03 vs. input pump power

The specific reference samples used in this thesis and the calibration process have been discussed in details in Appendix B

3.6 Optimized photo-thermal setup and detection limit

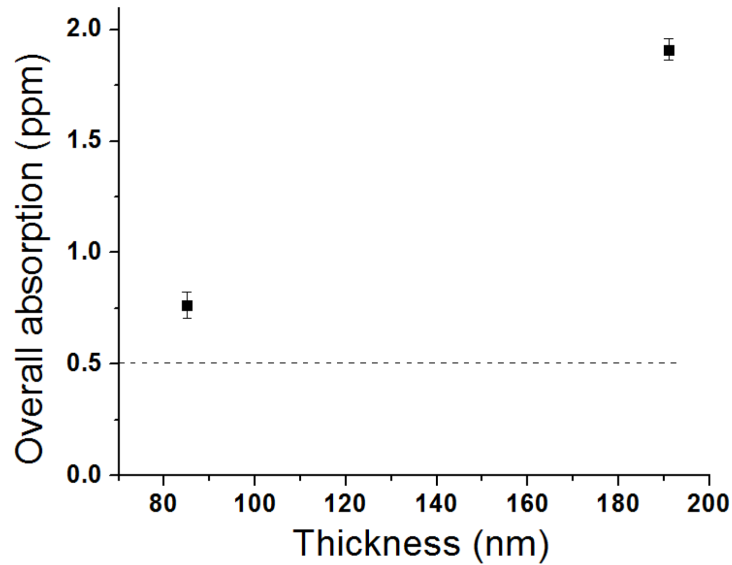

Figure 3.13: Absorption of two HfO_2 samples with different thicknesses

Figure 3.13 shows an example that with our current setup we can measure the absorption of samples larger than 0.5 ppm with a 1 W input power. The dash line represents the minimum absorption level that can be measured by our current photo-thermal setup.

3.7 Longitudinal scans of samples

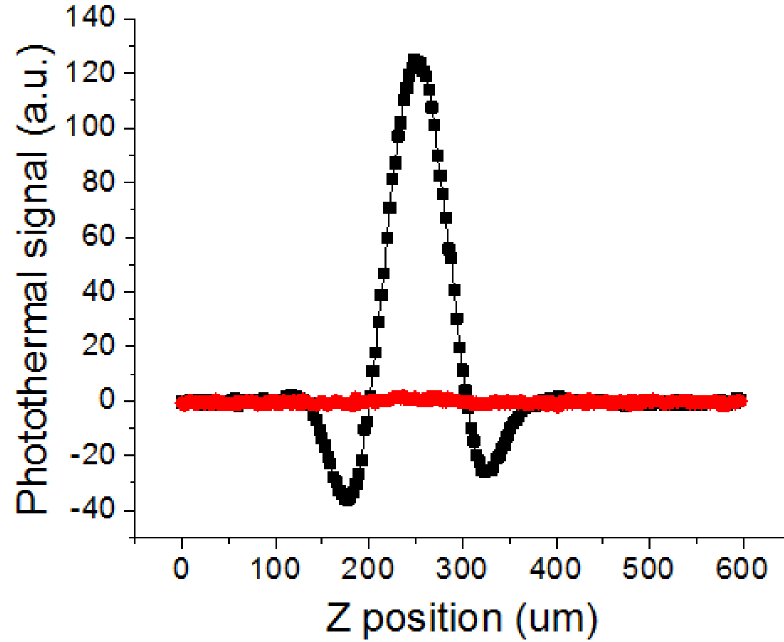

Figure 3.14: The longitudinal scan of as-grown HfO_2 with 200nm film thickness on a quarter inch fused silica substrate

The black curve shows the photo-thermal signal where the thin film move toward the pump/probe crossing point. The center peak corresponds to the position where the pump and probe beams cross at the thin film. The value for this maximum is used for calibration. The width of the central peak shows the longitudinal space resolution of the system, which is about 100μm. There are two side peaks with negative value because we measure X rather than R and the π phase shifts occur while crossing through those points. The red curve shows the photo-thermal signal where the substrate move toward the pump/probe crossing point. The signal is around the noise level of current setup, which is much smaller than that in the first case. The difference between two cases is that in first case the thin film absorbs the energy and creates a thermal lens in the substrate due to the heat flow, however, in the second case, the substrate absorbs the energy and creates a much weaker thermal

lens in the substrate due to very small absorption of fused silica compared to the HfO_2 thin film with 20 ppm. Therefore we can distinguish the thin film absorption from substrate.

3.8 Summary

In this chapter, setup parameters such as pump/probe beam size ratio, detection distance, probe focus to sample distance z' and iris size have been optimized for building a good photo-thermal setup with $\sim$0.5 ppm sensitivity, which has normalized to 1 W input power, 18μm transverse spatial resolution and 100μm longitudinal spatial resolution. Even better sensitivity is possible if noise from probe laser source can be reduced.

Chapter 4

Time resolved absorption of thin films

Optical coatings have been an area of intense research for decades [30]. Oxide films are the dominant material in the visible to near-IR spectral range due to their environmental robustness and low absorption, because of their large bandgap relative to the photon energy. The connection between the fundamental damage threshold and multiphoton ionization processes has been established by single-pulse subpicosecond-laser-damage studies [19]. However, the practical limit (i.e. the multiple-pulse damage threshold) is lower than the fundamental value[31]. This observation has been attributed to material changes arising from sub-threshold excitation of electrons into native and laser-induced states in the band gap [[31], [19]].Corresponding laser damage models can explain the dependence of the damage fluence on the number of excitation pulses and their spacing [23]. Long lived laser induced material modifications are well known in dielectric bulk materials and are often associated with self-trapped excitons [32]. Time-resolved spectroscopy on thin films also indicate

that the film does not fully relax between pulses of a train[33]. *

The midgap model[23] predicts an increase in absorption due to the occupation of states near the conduction band. TiO_2 is a material well suited to demonstrate this effect. Because of its relatively small band gap, material modification induced by CW and pulsed illumination can be compared. If the presence of the pump-laser itself leads to changes in the absorption, it will be observed in changes in the photo-thermal signal. Pump-induced changes to absorption of TiO_2 films have been studied previously[35][36]. However, these two studies used a CW pump and were limited to irradiances of just 400 W/cm^2 and 2.2 kW/cm^2, respectively. In the latter case, a drop in the absorption was observed, which was attributed to laser annealing of the film[36]. In later work Wu et al. compared films prepared by electron-beam evaporation and ion-assisted deposition and found the latter to have a lower and more stable absorption [37].

In this section, we compare laser-induced material modifications by CW and pulsed (train of femtosecond pulses) for both IBS and EBE TiO_2 thin film coatings. However, the IBS film results would be discussed in details in this section, please refer to EBE film results in Appendix. G.

4.1 Ion-beam sputtering TiO_2 time-resolved results

The absorption behavior of two different TiO_2 film samples was investigated. They were prepared (1) by ion-beam sputtering(IBS) and (2) by electron beam evaporation(EBE). The IBS film was 496nm thick and had a refractive index of 2.39. The

*In this section, I copied most parts from the paper [34] due to my contribution to all the experimental data shown in this section.

EBE film was 115 nm thick and had a refractive index of 2.2.

For a given pump mode (CW or pulsed) the absorption (thermal lens signal) was monitored as a function of time for different excitation powers. A new spot on the sample was selected before the next data set was taken. To estimate the recovery time of the induced absorption the pump was blocked after a certain absorption change was reached and then unblocked briefly at certain intervals to probe the thermal lens.

Third-harmonic microscopy (THM) showed great potential for the inspection of nascent optical films, see for example[38]. This optical far-field microscopy has the potential for in situ monitoring of films during deposition and annealing. Figure 4.1 shows THM images of the IBS and EBE TiO2 films used in this study. The image contrast arises from local anisotropies, which are clearly more pronounced in the EBE sample. We attribute this to boundaries (interfaces) between film domains, for example grain boundaries, in the EBE sample.

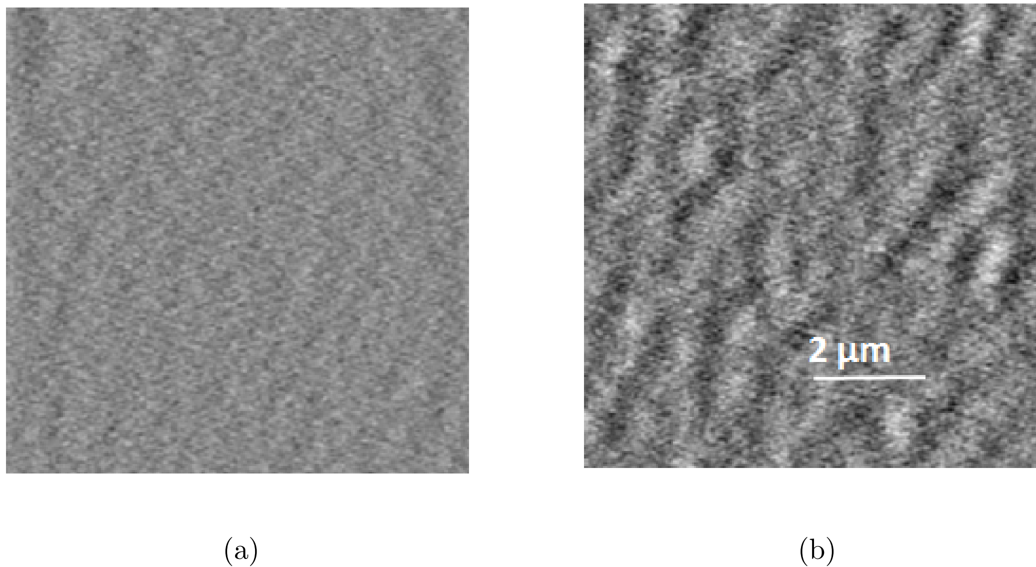

(a) (b)

Figure 4.1: Third-harmonic microscope images(10μm by 10μm)of (a) IBS and (b) EBE TiO_2 films [4]

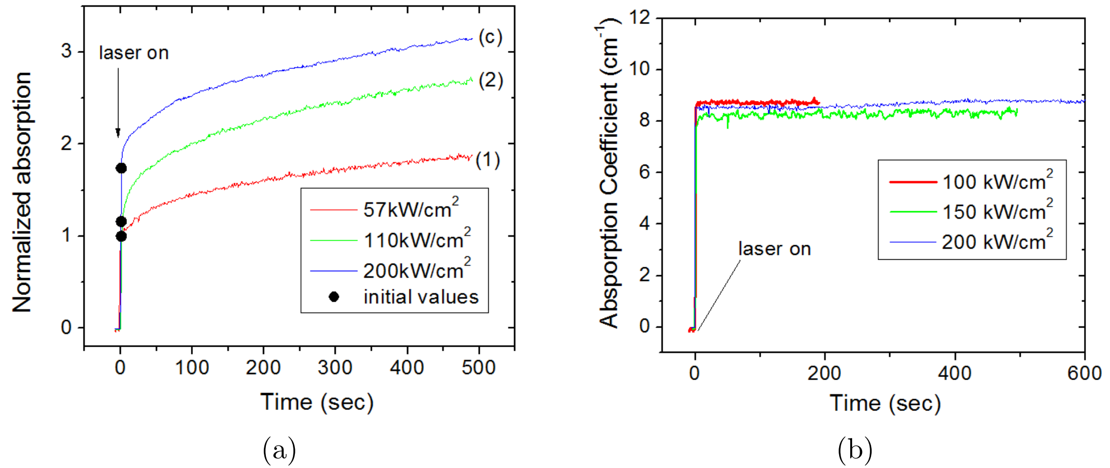

Figure 4.2: Time-resolved absorption of the IBS TiO_2 film for (a) pulsed illumination at (1) 57 kW/cm^2, (2) 110 kW/cm^2, and (3) 200 kW/cm^2 average irradiance; and (b) CW illumination

Figure 4.2a shows the time-resolved absorption for the IBS film at different irradiances when exposed to the femto-second pulse train. The data are normalized to the initial absorption measured at very low average power. The absorption increases monotonically over the exposure time. In contrast, the absorption for CW illumination is not time dependent for the incident powers used, see Figure 4.2b. The absorption value agrees with that measured for the initial absorption at low incident pulsed power. Figure 4.3 shows the initial absorption as a function of the power of the incident pulse train and the absorption value measured with the CW laser for comparison.

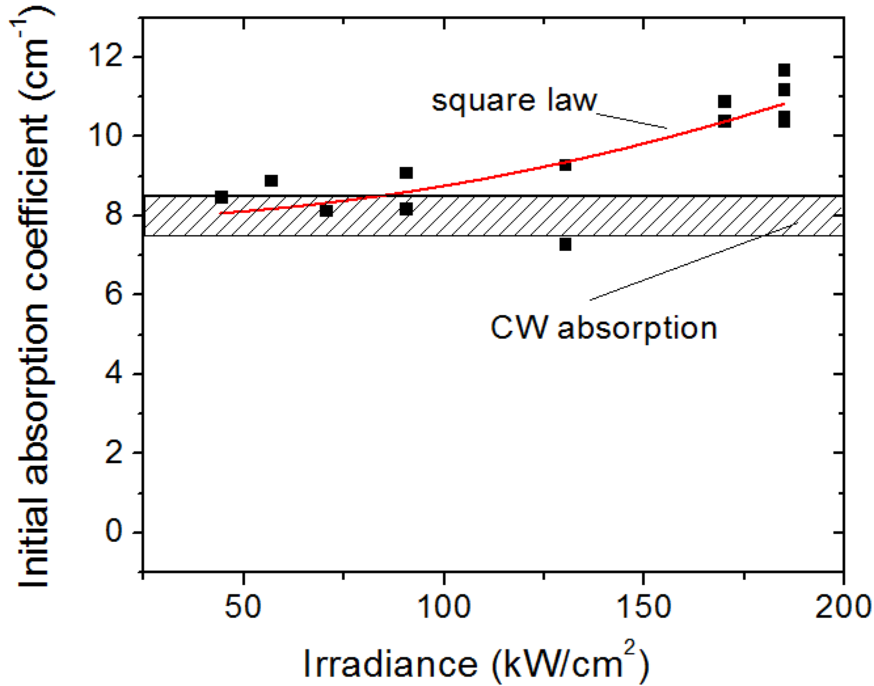

Figure 4.3: The initial absorption vs. the average irradiance for the IBS TiO_2 film under pulsed illumination. The absorption coefficient obtained with CW illumination is shown for comparison.

Refer to the model shown in chapter 2, we present it here(Fig. 4.4) again for simplicity. Both the IBS and EBE sample have an energy level, A_1, close to the valence band (VB), which is responsible for the absorption coefficient α_0. The quadratic dependence of the initial absorption coefficient on intensity under pulsed illumination,$\alpha_2 I^2$, is due to a three-photon absorption that can promote electrons to the CB(3h $\nu \approx$ 4.5 eV $> E_{gap} \approx$ 3.3 eV). From there these electrons can populate trap states $A_1$and A_2. Both of these states can absorb linearly and are responsible for the transient absorption component $\Delta\alpha$(t). In addition, they may increase the VB-CB absorption because they can represent near-resonant mid-gap states, which could enhance the multi-photon absorption coefficient.

The initial absorption coefficient derived from the measurements varies quadrat-

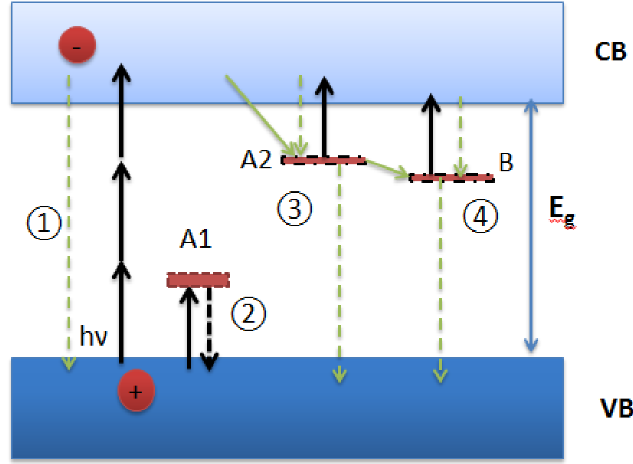

Figure 4.4: Simplified energy level scheme for TiO_2. (solid arrows = optical transitions; dashed arrows = relaxation processes.) Level A1, A2 is an existing trap state near VB and CB, respectively. B is a laser induced state.

ically with the incident power (intensity) of the pulse train, apart from a constant offset (α_0). These observations suggest that the absorption coefficient is the sum of an intensity dependent initial (t = 0) value α_i and an intensity and a time dependent component $\Delta\alpha$:

$$\alpha(I,t) = \alpha_i(I) + \Delta\alpha(I,t) \tag{4.1}$$

where the initial absorption coefficient for the IBS sample

$$\alpha_i(I) = \alpha_0 + \alpha_2 I^2 \tag{4.2}$$

has a constant contribution and a term quadratic in the incident intensity.

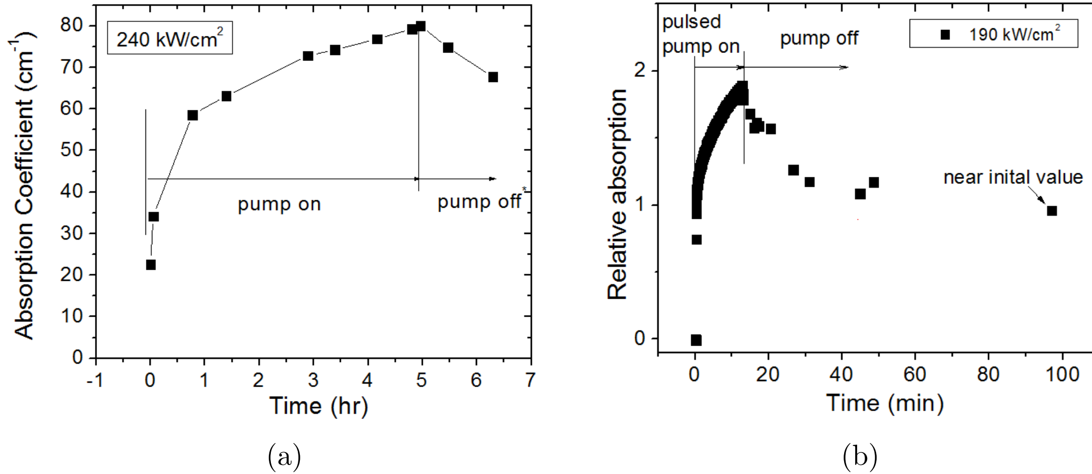

(a) (b)

Figure 4.5: Time-resolved absorption with relaxation for IBS film under pulsed illumination: (a) long-time scale; and (b) short-time scale

The distinction between states A_2 and B meant to explain the kinetics of the laser-induced absorption, both the increase to its maximum value and the relaxation after the pump is blocked. Figure 4.5a shows the absorption measured over 5 hours. The absorption increases rapidly over the first hour but then increases only another 33% over the next 4 hours, reaching a maximum value of 80 cm^{-1}. At that point the pump was blocked and the material was allowed to relax. Another two measurements were made over the next 90 minutes by unblocking the pump just long enough to measure the absorption and then blocking it again. During that time, the absorption had relaxed to 68 cm^{-1}. On the other hand, Fig.4.5b shows that the film, when exposed to the pump for just twelve minutes, relaxes to its initial value in under an hour. Therefore, the states A_2 are those that are quick to be filled and quick to relax while the state B take much longer to be filled and relax more slowly too. The states A_2 might be existing traps states whereas the B are laser-induced states. The final density of occupied B states depends on the pump intensity.

In summary, the laser-induced absorption observed in TiO_2 is caused by band-

to-band (VB-CB) excitation and the subsequent occupation of existing and laser-induced states near the CB. This excitation process is sensitive to the film micro-structure. In the EBE sample, the effective cross section for VB - CB excitation is greatly increased, presumably due to interface states, so that absorption changes occur even with CW irradiation. The lifetime of the induced absorption depends is different for the trap (minutes) and laser-induced state (hours), which can be controlled by the duration of the exposure and intensity. The proposed energy level diagram based on the absorption measurements exhibits similar features than that derived from multiple pulse damage measurements[23]. This supports the hypothesis that the occupation of native and laser-induced midgap states are responsible for the observation that the multiple-pulse laser-induced damage threshold is lower than the fundamental value measured by single-pulse testing.

4.2 Absorption reduction by laser conditioning and thermal annealing

Laser conditioning is a process where an optic is illuminated at a progressively higher influences to obtain absorption reduction, thus leading to the increase of optics laser damage threshold[39, 40]. And it has been shown that laser conditioning has improved the laser damage threshold of some optical coatings by more than a factor of 2[5]. Similarly post deposition annealing also leads to reduction in absorption and increased damage threshold[41].

Time dependent absorption was measured for HfO_2 films prepared by ion beam sputtering. A total of four films with different thicknesses and/or post-deposition treatments were prepared. These are listed in Table. 4.1. Samples A and B were from the same coating run, and sample A was tested as grown while sample B received

an additional post-deposition annealing treatment. Similarly samples C and D were tested as grown and after annealing respectively. Figure 4.6 shows the time dependent absorption of samples A and B. The absorption of the as-grown film, sample A, drops from its initial value of 26 ppm to its final value 8 ppm. On the other hand, the absorption of the annealed film, sample B, is nearly constant at 1 ppm.

label	Coating ID	thickness (nm)	post deposition
A	130220b	85	as grown
B	130220b	85	annealed
C	130222b	191	as grown
D	130222b	191	annealed

Table 4.1: List of samples and corresponding labels in this thesis

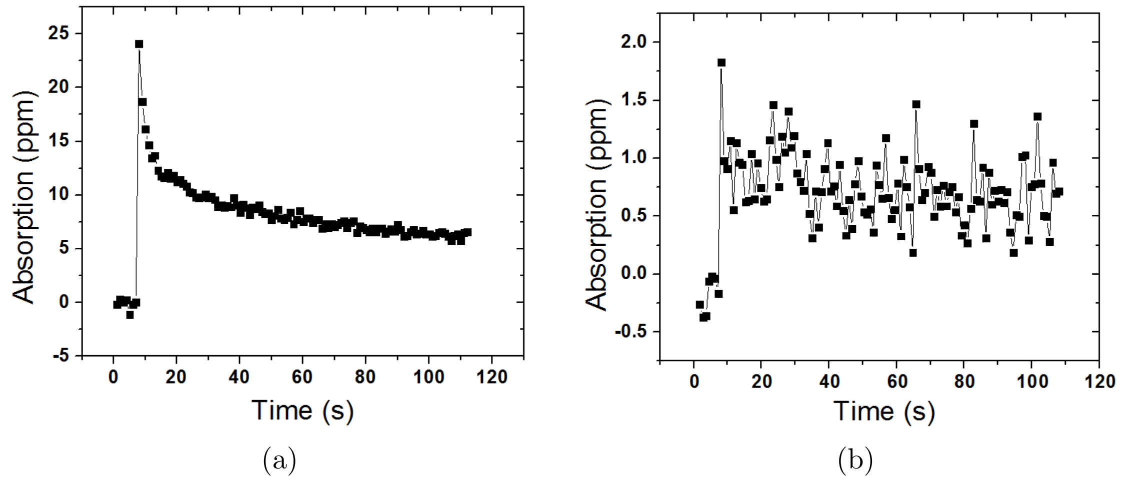

Figure 4.6: Absorption of as-grown and annealed HfO_2 samples respectively vs.time at a local spot under 532nm CW excitation with intensity $990kW/cm^2$.

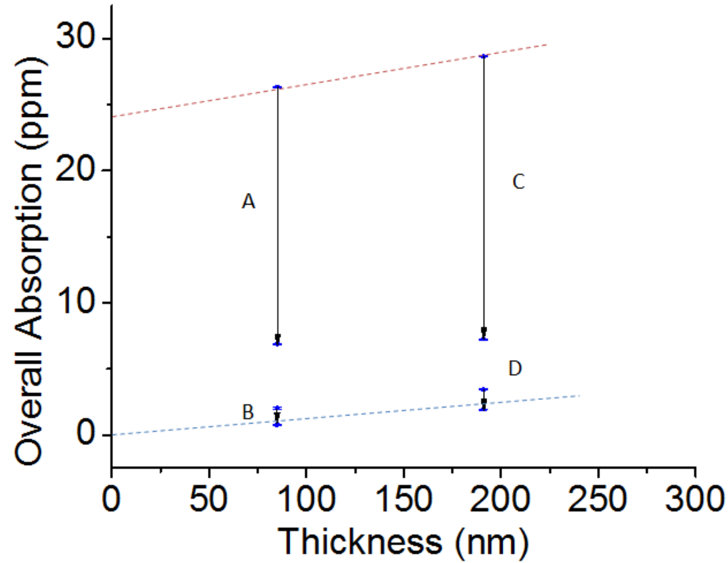

Figure 4.7: The initial and final absorption of annealed and as-grown HfO_2 with different film thickness. The arrows indicate the changes.

Figure 4.7 shows the initial and final absorption vs. thickness for all four samples. The absorption of the annealed films extrapolates to zero for zero film thickness. But the dashed line through the initial absorption of the as-grown films does not approach zero for zero film thickness. This result indicates the absorption at the interfaces (film-air and/or film-substrate). Figure 4.8 shows calculated absorption vs. thickness where α is the volume absorption coefficient and γ is the interface absorption coefficient. The calculations are discussed in details in Appendix J. This curve goes through both experimental values. The contributions of the volume and interface to the total absorption are listed in Table 4.2 for both thicknesses.

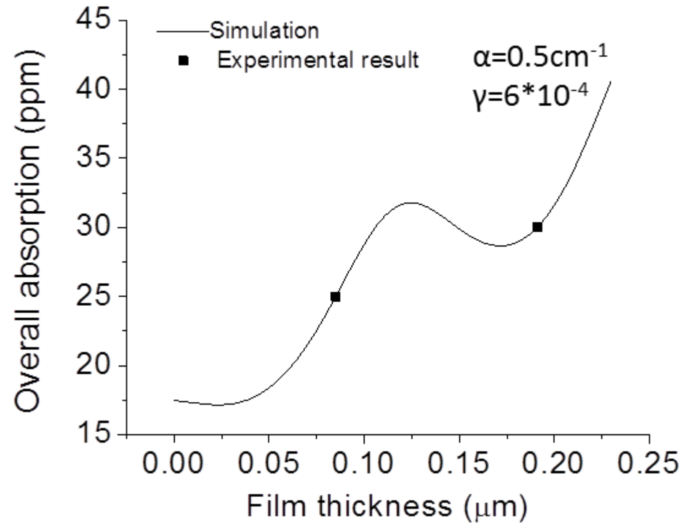

Figure 4.8: The theoretical and experimental absorption results vs. film thickness

In Figure 4.8, we define α as the volume absorption coefficient and γ the interface absorption coefficient.

	Interface	Volume
Extinction coefficient	$6*10^{-4}$	0.5 cm^{-1}
Absorption of sample C (ppm)	19	11
Fraction of overall absorption	63%	37%
Absorption of sample A (ppm)	19	6
Fraction of overall absorption	76 %	24%

Table 4.2: Absorption coefficients of interface and volume, associated with corresponding absorption of sample C and A with different film thickness.

In Table 4.2, it turns out that the interface absorption will no longer be negligible but dominates in the as-grown film samples.

In summary, the time dependent absorption of both annealed and as-grown HfO_2 with different film thicknesses has been investigated under 532 nm CW laser. The absorption of as-grown film decreases with illumination time while annealed one

is independent of time. The thickness dependence of the absorption indicates the as-grown films have a significant interface component, whereas the annealed films exhibit just volume absorption. Therefore we conclude that the laser conditioning effect observed in the as grown films is due to reduction of interface state density, just like the post-deposition annealing process. So compared to as-grown films, the annealing process has improved the dielectric films in these ways :(1) It reduced overall absorption and time dependent issue effect.(2) It limited the interface absorption effect.(3) It could reduce defects both in thin films and substrate surfaces which could be discussed in details in chapter 5.

Chapter 5

Combined absorption and scattering imaging

Laser damage in optical films by nanosecond laser pulses are initiated at localized defects[42]. In this chapter we demonstrate the use of the photo-thermal setup for mapping localized absorption and scattering centers in optical films as potential damage precursors. The sample is raster-scanned (see Fig. 5.1)and single-point measurements are combined to form absorption and scattering maps. The resolution of these maps is limited by the focused pump size(FWHM=18 μm).

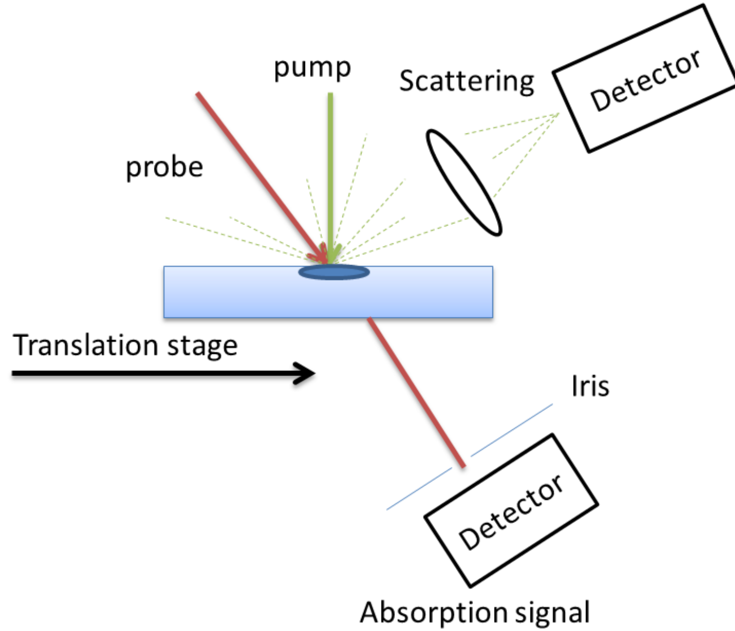

Figure 5.1: A layout of setup for simultaneously collecting scattering and absorption signals.

5.1 Sc_2O_3 scanning results

Sc_2O_3 films prepared by ion beam sputtering on fused silica substrates are used to demonstrate simultaneous absorption and scatter mapping. Fig. 5.2 shows absorption and scattering maps for a scandia film under 1 watt CW pump laser.

From these images, one can conclude that there are at least three different kinds of sites: (1) There are the sites with strong absorption associated with strong scattering.(2) There are sites where there are strong absorption but no scattering.(3) There are sites with strong scattering but no strong absorption.These would be three different kinds of defects, and they might or might not affect the laser damage threshold measurements at the end, thus more work is needed to prove that. Dust particles are not a problem, see Appendix E.

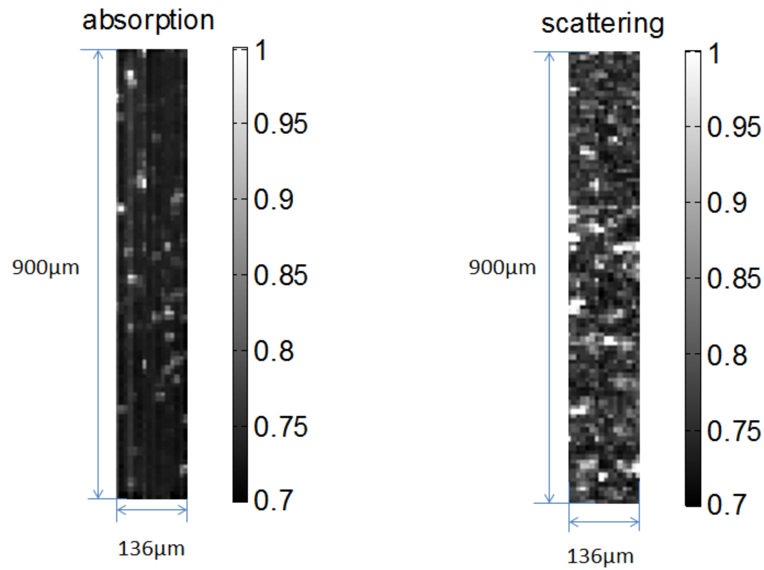

Figure 5.2: Left : Absorption image of Scandia with pump intensity 220kw/cm^2. Right : Scattering image of Scandia. The size of both images is 900μm $\times$ 136 μm and each pixel is 9μm $\times$9μm.

Fig. 5.3 shows three consecutive line scans. We observed that in Fig. 5.3a the absorption of thin film decreases in the second and third scan lines because of the laser conditioning, but the two spikes remain the same. And the scattering measurements are the same for the three successive scans.

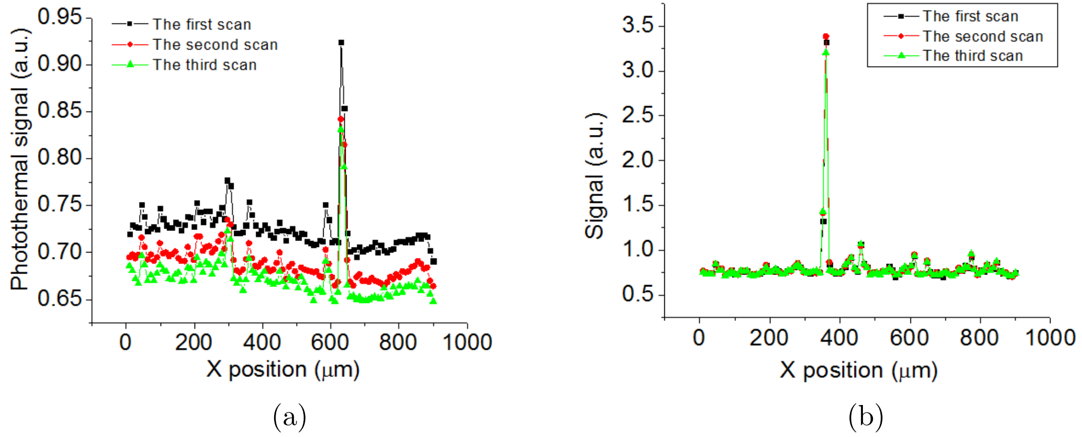

Figure 5.3: Three successive lateral line scans of Scandia film showing (a)absorption (b) scattering.

5.2 HfO_2 scanning results

To further investigate whether the spikes come from the thin film or substrate, we statistically analyze the spike density on both side of sample. For safe argument, we have assumed that both sides of substrate are identical. And the back side of sample refers to the substrate side. Thus, we scanned a couple of lines on the film and substrate side.

For a pair of HfO_2 sample with 191 nm thickness, lateral scan for both film and back side have been tested, see in table 5.1 For a pair of HfO_2 sample with 85 nm thickness, lateral scan result can refer to Appendix. H.

	D substrate	C substrate	D Film	C Film
Spike#	3	5	1	5
Scan area (mm^2)	0.14	0.14	0.14	0.41
Absorption density (mm^{-2})	21	36	7	12
Spike absorption (ppm)	1	1.2	1	16

Table 5.1: Scanning results for sample D(annealed) and C(as-grown)

Compared with annealed sample, the spike density tends to be larger in as-grown sample both for film and substrate side, which is independent of film thickness. In both as-grown and annealed samples, we also found more spikes on substrate surfaces with about 2 times larger than that on film side.

In summary, with current photo-thermal lens geometry we can identify several kinds of localized defects by combining the scattering measurements. The annealing process reduced both the spike density and absorption on thin film and substrate side.

Chapter 6

Summary

The fact that absorption in real optical films is possible for photon energies well below the band gap because of defects that result from the thin film deposition process has been discussed. The photo-thermal setup with sensitivity of ∼0.5 ppm is developed and optimized using modeling and experiments. The setup is calibrated using a film with known absorption deposited on fused silica substrate, the same substrate of the test films. The photo-thermal setup provides us a direct way to detect, localize and characterize the defects in optical thin films since it is important for developing high quality mirrors in high power lasers. Three examples are applied to demonstrate that. First, the laser-induced absorption in ion beam sputtered TiO_2 is investigated. Second, the effect of laser conditioning and thermal annealing on the absorption of HfO_2 is presented. Third, simultaneous mapping of absorption and/or scattering sites is shown as well as the density of these sites is estimated.

Appendices

A Experimental Procedures **1**

B Lists of reference sample **2**

C How reproducible of the calibration sample experiment **3**

D Conversion of absorption coefficient from absorption **4**

E Absorption and scattering from dust **5**

F Substrate issue **6**

G Electron beam evaporation TiO_2film results **7**

J Overall absorption calculation for the sample with a single layer film **8**

Appendix A

Experimental Procedures

The photo-thermal setup has been aligned in such a way that anyone who follows the routine shown in the following context can align the setup in a couple of minutes.

1. Check probe power to make sure probe laser works in a stable power mode.
2. Check pump power. If using a tunable laser such as the Ti:Sapphire oscillator, then check the spectrum.
3. Align both probe and pump beam through irises on the experiment table.
4. Use the $\sim 20\ \mu$m pinhole to overlap both beams as shown in Fig. A.1

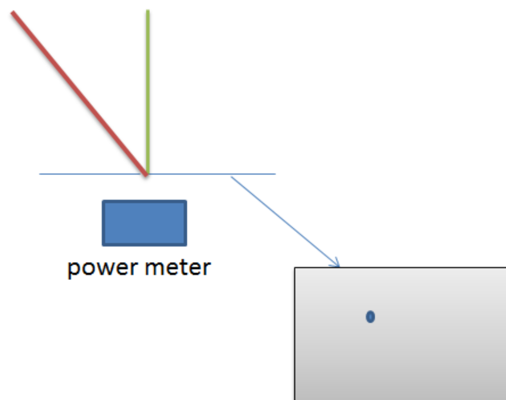

Figure A.1: The schematic of aligning beams with the pinhole

5. Insert the pinhole into the sample holder, and adjust the xyz axes to find the focal point of pump beam by maximizing the power that passes through the pinhole.

6. Find the focus of the probe beam by moving the pinhole in x and y (do not touch z) by maximizing the throughout using the power meter.

7. Now overlap pump and probe by adjusting the pump focus lens in x and y to one again maximize the power through the pinhole.

8. Replace pinhole with reference sample, and reduce pump power to the level such that ΔS on the lock in amplifier goes to noise level without using iris before photo-detector, where ΔS is the voltage on the Lock in amplifier representing probe intensity change at the reference frequency.

9. Make reference to the calibration samples and powers listed in Appendix B.

10. Turn chopper on , minimize the iris which locates before the photo-detector and adjust reference sample in z axis to get maximum ΔS.

11. Adjust pump lens holder in x-y axis to get higher ΔS if necessary. Move probe lens holder in the direction of probe beam if the setup is to align for a new

laser system. Then fix the probe lens holder without changing the position and angle with respect to the direction of pump beam.

12. Record the input pump power, sample holder z, ΔS and S for calibration samples, where S is the voltage on the oscilloscope.

13. Day to day reproducibility of the z position is within the range of 75 μ m.

14. Replace the reference sample with ground glass slide (one surface has rough surface but the other one does not) and align the scattering light to photo-detector.

15. Use power meter to measure the scattered light before photo-detector P_{sc}, and record voltage V_{sc}on the lock-in amplifier.

16. Replace the reference sample with test sample and increase the pump power. adjust test sample in z axis until one founds the maximum ΔS.

17. On the lock-in amplifier, we usually choose X quadrature for the ΔS, and we need to press the auto-phase button repeatedly everytime when we make our experiments.

18. For optimum operation, we usually choose 1.1kHz with 300 ms time constant on the lock in amplifier, more details can be found in Chapter 3.

Appendix B

Lists of reference sample

Following the procedure in Appendix A, one records three values for a given measurement: the AC signal, the DC level, and the pump power. Because the AC signal is proportional to the pump and probe powers, the photo-thermal signal is calculated as Eq. I.9

$$\Delta = \frac{\Delta S}{S} \tag{B.1}$$

In order to convert to the total absorption, the reference sample with the following two properties is required: (a) the absorption of the reference film must be known; (b) the reference film must be on the same substrate as the unknown. The absorption of the unknown is then calculated using Eq. B.2

$$Q = \frac{\Delta}{P * A} \tag{B.2}$$

where Q is called the calibration factor.

There were two reference samples used for calibrating the absorption measurements at 532 nm. These are listed in table. B.1

The Calibration power for NDF03 is needed to be reduced in the future in order to avoid refractive index change.

	NDF03 with BK7	AlO_x with fused silica
Absorption	0.4	0.57
Calibration factor (μm/ppm)	1.5	0.5
Calibration power (mW)	5	0.6

Table B.1: Calibration samples on different substrate with 532 nm

The AlOx reference sample was also used to calibrate the measurements done at 800 nm. In that case, there was a difference absorption measured for pulsed and CW excitation. The calibration values are listed in table. B.2

	Pulsed	CW
Absorption @ 800 nm	0.3	0.35
Calibration factor(μm/ppm)	0.61	0.74
Calibration power (mW)	5.3	4.2

Table B.2: Calibration sample AlO_x on fused silica under CW and pulsed excitations round 800 nm

Appendix C

How reproducible of the calibration sample experiment

One can easily align the photo-thermal setup in the way shown in appendix A. However, we got different calibration values every time when we aligned the setup, see Figure.C.1

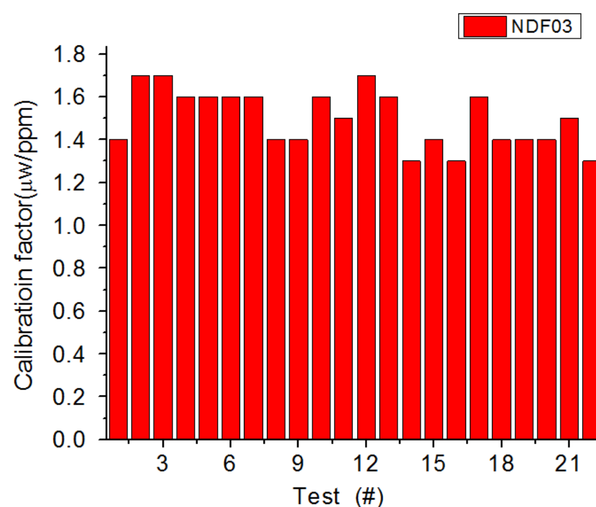

Figure C.1: Calibration factor of NDF03 reference sample measured on different days

The accuracy of the calibration depends on the uncertainty of the calibration coefficient. Fig. C.1 shows a plot of the calibration coefficient of the NDF03 reference sample measured on different days. The average calibration factor is 1.5 μW/ppm with standard deviation of 0.13, giving an accuracy of roughly 9%.

Appendix D

Conversion of absorption coefficient from absorption

The photo-thermal instrument measures the total absorption of the film, which depends on the film thickness amongst other parameters. Instead we report the absorption coefficient, which comes from the Beer-Lambert law that describes the intensity of light traveling in one direction through an absorber. The conversion from total absorption to absorption coefficient is complicated in thin films due to reflections at the air film and film-substrate interfaces which lead to the Fabry-Perot effect.

With three given refractive indices: n_1,n_2,n_3 and a film thickness d. We can calculate reflection coefficients at air film and film substrate interfaces ρ_{12},ρ_{23}. The round trip propagator G can be defined as

$$G = e^{-\alpha * d} \tag{D.1}$$

G is less than 1 since the film do not have gain but loss in this case. Take the thin film as a resonant cavity, and the transmission and reflection could be expressed

as[28],

$$T = \frac{G(1-\rho_{12})(1-\rho_{23})}{(1-G\sqrt{\rho_{12}\rho_{23}})^2 + 4G\sqrt{\rho_{12}\rho_{23}}sin^2\theta} \tag{D.2}$$

$$R = \frac{(\sqrt{\rho_{12}-\rho_{23}})^2 + 4G\sqrt{\rho_{12}\rho_{23}}sin^2\theta}{(1-G\sqrt{\rho_{12}\rho_{23}})^2 + 4G\sqrt{\rho_{12}\rho_{23}}sin^2\theta} \tag{D.3}$$

$$A = 1 - T - R \tag{D.4}$$

Since the absorption is so low that within the initial linear region in Fig. D.1 we can define a correction factor as in Eq. D.5

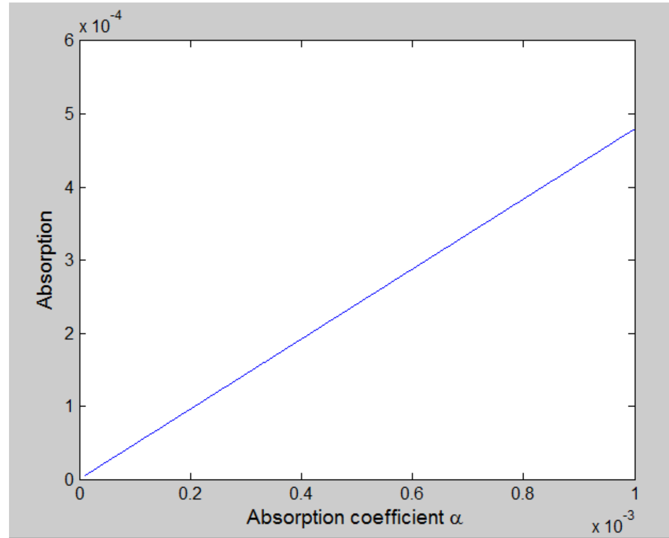

Figure D.1: Absorption vs.α for a given film index and thickness

$$Q = \alpha/A \tag{D.5}$$

Since $A$is function of the parameters such as refractive index n and thickness l of thin film, Q will be dependent of both n and l. Therefore, we can calculate any absorption coefficient of thin film with given n and d.

Appendix E

Absorption and scattering from dust

There are a few spikes while we laterally scan the thin film. Therefore we need to make sure that the spikes are from thin film itself before making any conclusion about that. The first thing we need to pay attention to is the dust. Is it known that the dust is everywhere, and it would adhere to the surface of any optical components if some of them have static charge to them. We set up a Nitrogen flow dust cleanser which could try to get rid of dust around the test surfaces, check the Figure. E.1

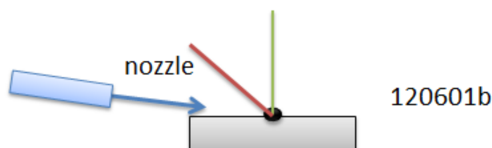

Figure E.1: The layout for the Nitrogen flow setup

But it turns out that it could not get rid of dust but cause additional noise with high flow rate, one could found in the Table. E.1

	Mean absorption (ppm)	Standard Deviation
High flow rate	0.78	0.4
low flow rate	0.7	0.2
No flow rate	0.76	0.17

Table E.1: Mean absorption and standard deviation measured at the same spot with different flow rates

It not only causes additional noise but also adds dust to the surface, see Figure. E.2

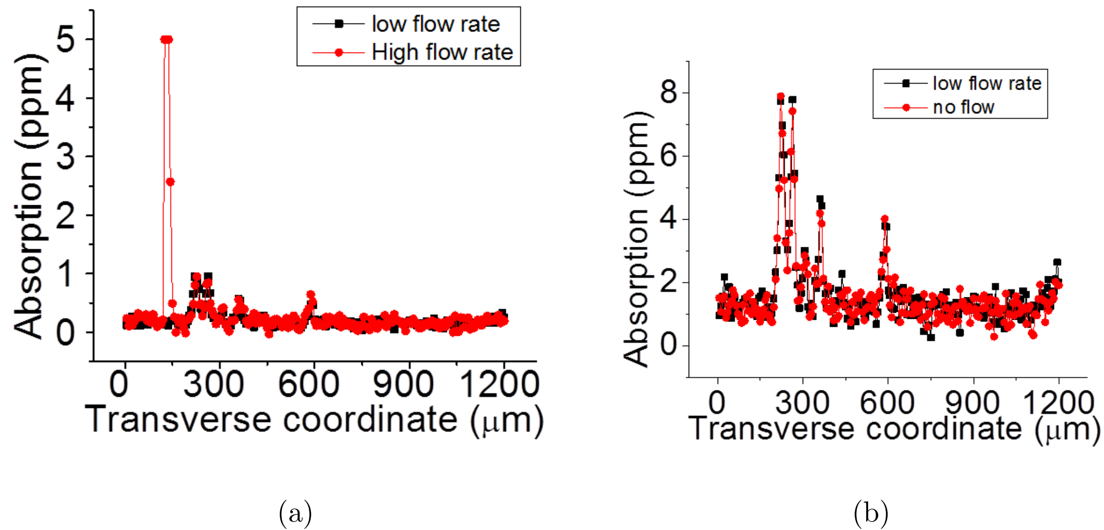

(a) (b)

Figure E.2: (a)The lateral scan of a same line with low flow rate first and then high flow rate.(b)Lateral scan of a same line without flow rate and then with low flow rate.

There is no obvious spikes in the first lateral scan under low Nitrogen flow rate, but a huge spike exists the second time with high flow rate. Based on above results,

we could not run this kind of experiment under high flow rate since everything will messes up. Then we lower the flow rate in Figure (b), the two scan lines are overlap with each other and make no difference, indicating no effect by the Nitrogen flow. In this experiment, we tried to use high flow rate and low flow rate and no evidence to show that using Nitrogen flow can prevent dust from the sample surface without leading to additional noises.

Checking the lateral scan spikes on a dusty sample is an alternative way to exclusive the dust problem from our scanning results. We can see how the dust effects the absorption and scattering lines on a sample surface. Therefore, a cleaned substrate was left uncovered over night. Dusts may adhere to the surface of the substrate. The following graphs Figure. E.3 show how the dust behave in both absorption and scattering scanning lines

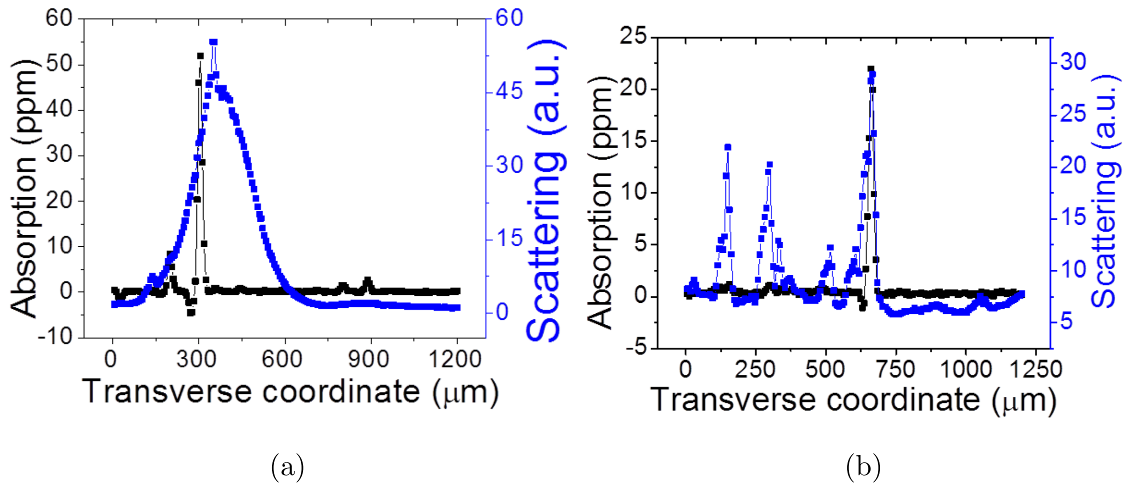

(a) (b)

Figure E.3: (a)(b)Scanning lines of both absorption and scattering at two different places.

From Figure. E.3 we see that the absorption spikes are about 10 times larger, compared with the absorption spikes on a cleaned sample surface. Secondly, there are scattering associated with absorption spikes. Finally, there are scattering without

absorption but no absorption without scatter. The possible reason would be that dust would absorb energy without transferring it to the sample surface or even could not absorb energy of the laser.

The dust absorption and scattering lines distinguished from that of clean surfaces in such way, it should not effect spike detection after carefully cleaning.

Appendix F

Substrate issue

In appendix E, we discuss about if dust would effect spike detection. In this section, we also need to pay more attention to the substrate surfaces, since it also could be one of the spike sources. We usually assume that the front surface which attaches to the thin film is identical to the surface on the backside. The fused silica substrate discussed in this chapter are listed in Table F.1

Sample	Label
HfO_2 120602 b substrate	I
HfO_2 130222 b substrate	J

Table F.1: The fused silica from different vendors

Absorption measurements of sample I is shown in Figure F.1.

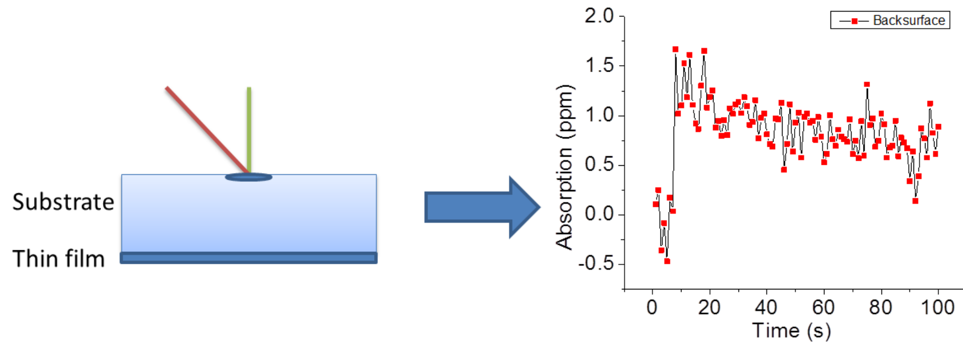

Figure F.1: left: Time dependent absorption measurement layout. Right: The absorption of sample I vs time

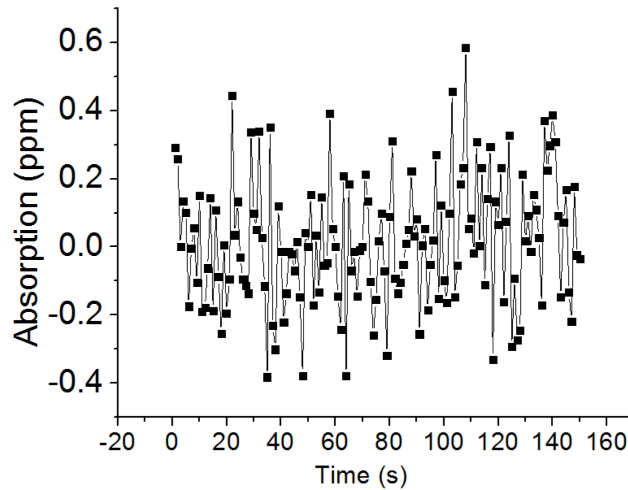

Figure F.2: The absorption of sample J vs time

The substrate absorption in Fig. F.1 is larger than that in Fig. F.2. They are both fused silica, but provided by different vendors. Referring to the longitudinal scan result in Figure. F.3, we can see that the absorption just occurs at the substrate surface, which could be caused by contamination.

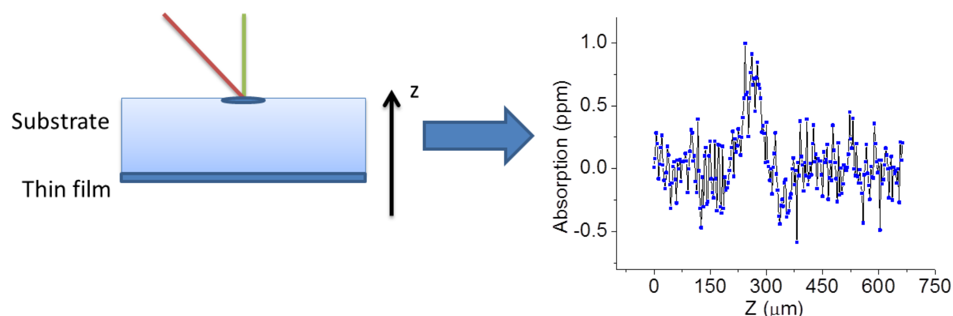

Figure F.3: left: Longitudinal scan measurement layout. Right: The absorption of sample J vs longitudinal position Z.

We sent them back to our co-workers in Colorado State University. They cleaned that and sent it back to us. We tested again and the result is shown in Fig. F.4

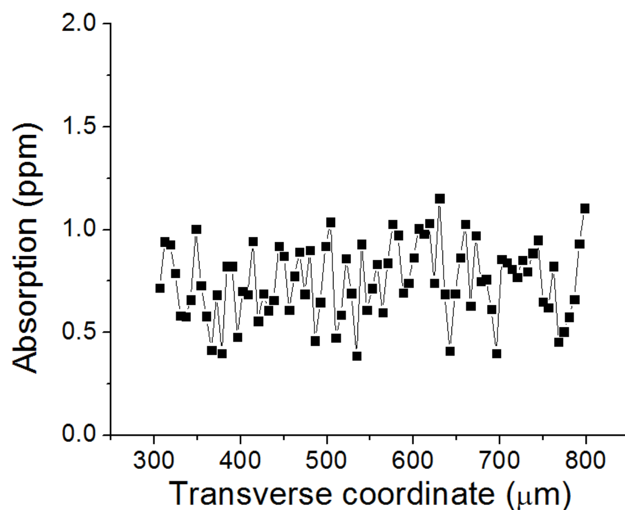

Figure F.4: Lateral scan of cleaned sample I

The average absorption is smaller than that in Fig. F.1, but it is still above the detection limit of our current system(0.5 ppm).

Appendix G

Electron beam evaporation TiO_2 film results

We used IBS sample as an example to demonstrate the effect that the increased absorption is due to the occupation of states near the conduction band. The EBE film is presented here for a comparison.

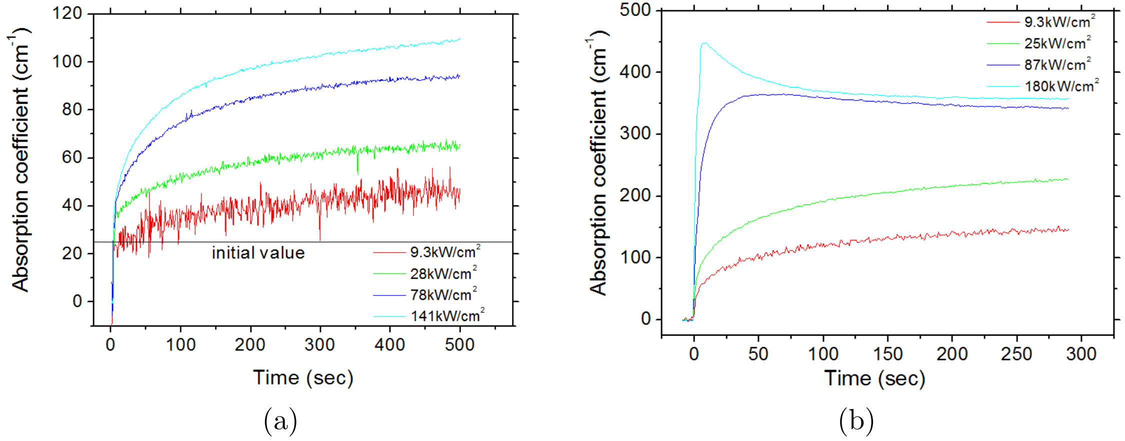

Figure G.1: Time-resolved absorption coefficient for the EBE film under (a) CW illumination at (1) 9.3 kW/cm^2, (2) 28 kW/cm^2, (3) 78 kW/cm^2, and (4) 141 kW/cm^2 irradiance; (b) pulsed illumination at (1) 9.3 kW/cm^2, (2) 25 kW/cm^2, (3) 87 kW/cm^2, and (4) 180 kW/cm^2 peak irradiance.

For the EBE film, the absorption exhibited a time-dependent component, $\Delta\alpha$ for both CW and pulsed excitation, see Fig. G.1. The results for CW excitation of the EBE film (FigureG.1a) were similar to the pulsed illumination of the IBS film, monotonic increase of the absorption with power dependence. In the case of pulsed excitation (Fig. G.1b) the absorption increase is faster and a new feature appears at the highest irradiances, a transient spike in the absorption.

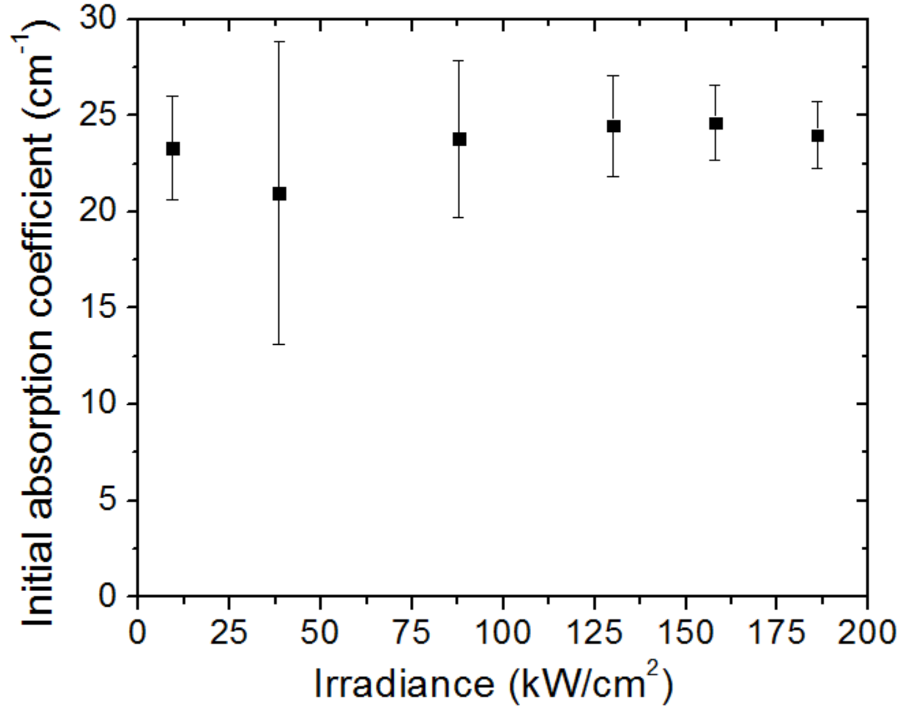

Figure G.2: Initial absorption vs. irradiance of EBE film under CW illumination.

Fig. G.2 shows the initial absorption of the EBE film under CW illumination. Within the error of the measurement, the initial absorption coefficient(α_0 24cm^{-1}) does not depend on the CW power and is about three times larger than for the IBS film. The functional behavior of α_i(I) could not be determined from the pulsed illumination data, because the change in the absorption was too rapid at high irradiances to get reliable values for the initial absorption. More details about EBE films have been discussed[34].

Appendix H

Spike distributions of HfO_2 C and D

Label	side	Spike#	Scan area(mm ^{2})	density (mm^{-2})	spike absorption(ppm)
HfO_2B	Back	0	0.3	0	0
HfO_2A	Back	9	0.18	50	8
HfO_2B	Film	1	0.3	4	20
HfO_2A	Film	5	0.27	24	6

Table H.1: Scanning results for annealed and as-grown HfO_2 with 85 nm thickness

Appendix I

Model of photo-thermal signal

The case of a pulse-laser excited sample probed with a continuous laser is examined first. Photo-thermal lens signals are calculated by first finding the time-dependent temperature change resulting from instantaneous sample excitation[18]. The expression for the temperature change in the sample as a function of radius and time can be obtained by the solution of the heat transfer equation[25]

$$\rho C_\rho \frac{d[\Delta T]}{dt} - \kappa \nabla^2 [\Delta T] = U(r,t) \tag{I.1}$$

where ρ and C_ρ are density and heat capacity of the thin film respectively. The first term on the left-hand side equation represents the time rate of change of energy stored in a unit volume, the second term on the left-hand side would be the rate of energy entering or leaving through the boundary surface of the volume, and the term on the right-hand side shows the heating due to the absorption which is described by

$$U(r,t) = \delta(t)\alpha H(r) \tag{I.2}$$

where α is the absorption coefficient, $\delta(t)$ is the delta function, and H(r) is the fluence for a TEM_{00} Gaussian excitation pulse,

$$H(r) = \frac{2E}{\pi w_e^2} exp(\frac{-2r^2}{w_e^2}) \tag{I.3}$$

E is the pulse energy, w_e is the excitation-beam radius, and r is the radial distance from the beam center.

After the integration is performed, the solution of EquationI.1 gives the time-dependent temperature change

$$\delta T(r,t) = \frac{2\alpha E}{\pi w^2(t)\rho C_\rho} exp \frac{-2r^2}{w^2(t)} \tag{I.4}$$

w^2(t)= $w^2(1+2t/t_c)$ is the time dependent radius of the temperature change, and t_c is a characteristic thermal time constant of the medium.

Next the radially dependent optical phase shift produced by this temperature change is found,

$$\varphi(r,t) = \exp[i\varphi] = \exp[ikl\Delta n] \tag{I.5}$$

where φ is the phase shift, k is the wave vector of probe beam and l is the sample path length. In particular, Δn is the index change caused by the temperature change associated with the thermal-optical coefficient dn/dT,

$$\Delta n = \Delta T \frac{dn}{dT}. \tag{I.6}$$

Finally, the phase shift is subsequently used to find the the effect on probe laser beam after passing through the sample. The electric field of probe can be obtained by multiplying the phase shift with incident electric field. And by performing the integration in diffraction calculations, we obtain the electric field at the detection plane with a distance d away from sample.

Two approximations have been reasonably introduced before giving the final analytical expression for the diffractive photo-thermal signal[44]. The first is the iris

approximation. The model assumes that the iris size is vanishingly small. So we look at the intensity change at r=0. The other approximation is for the exponential phase shift. Since it is claimed in Sheldon[44] that because the induced phase shift in most photo-thermal lens experiments is much less than 1, the phase shift can be given as

$$exp(i\delta\varphi) \approx 1 + i\delta\varphi \tag{I.7}$$

where higher-order series approximations are ignored in this case.

The photo-thermal lens signal is defined as the relative change of the probe intensity with and without the thermal lens effect. Thus the analytical expression can be defined by

$$p = \frac{\Phi(t) - \Phi(\infty)}{\Phi(\infty)} \tag{I.8}$$

where $\Phi(t)$ represents the probe intensity with laser excitation, and $\Phi(\infty)$ is the probe intensity with material relax for enough time. Thus no thermal effect would be considered in this case. The final analytical expression for the photo-thermal signal estimated in [18] with all the setup parameters,

$$p \approx \frac{-8dkw^2(t)\varphi(t)(z_p^2 + z\prime^2 + dz\prime)}{k^2w^4(t)(z_p^2 + z\prime^2 + 2dz\prime + d^2) + 8kw^2(t)d^2z_p + 16d^2(z_p^2 + z\prime^2)} \tag{I.9}$$

Where $z\prime$ is the probe focus to sample distance, z_p is the Rayleigh range of probe laser, d is the sample to iris distance and $w(t)$ is the time dependent radius of the temperature change.

Appendix J

Overall absorption calculation for the sample with a single layer film

For the sample with thin film on top of substrate, we define four layers in Fig. J.1

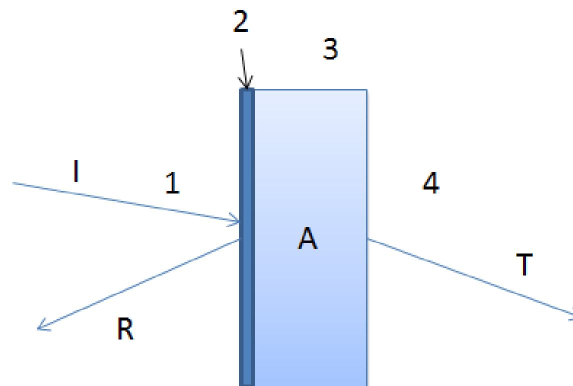

Figure J.1: The schematic graph shows that the incident beam can be reflected , absorbed and transmitted by the test sample.

This calculation adds a minor adjustment of matrix formalism for modeling the multiple-beam interference [45].

The reflection coefficients at each interface can be calculated by,

$$r_{jk} = \frac{n_j - n_k}{n_j + n_k} \tag{J.1}$$

and the transmission coefficients at each interface can also be expressed as,

$$t_{jk} = \frac{2\ n_j}{n_j + n_k} \tag{J.2}$$

where $k = j + 1$,$j = 1, 2, 3$.

The phase shifts within film and substrate are given by,

$$\beta_{2,3} = \frac{2\pi\ n_{2,3} d_{2,3}}{\lambda}. \tag{J.3}$$

The interface transition matrices are given by,

$$\text{H}_{jk}= \begin{matrix} \frac{1}{t_{jk}} & \frac{\gamma_{jk}\ r_{jk}}{t_{jk}} \\ \frac{\gamma_{jk}\ r_{jk}}{t_{jk}} & \frac{1}{t_{jk}} \end{matrix}$$

where $k = j + 1$,$j = 1, 2, 3$.

The layer propagation matrices for layer 2 and layer 3 are given by,

$$\text{L}_{2,3}= \begin{matrix} e^{-i\beta_{2,3} - i\alpha_{2,3} d_{2,3}} & 0 \\ 0 & e^{i\beta_{2,3} - i\alpha_{2,3} d_{2,3}} \end{matrix}$$

Then the stack matrix is given by,

$$B = H_{12} * L_2 * H_{23} * L_3 * H_{34}. \tag{J.4}$$

The total reflection R can be obtained by

$$R = |\frac{B_{1,2}}{B_{2,2}}|^2. \tag{J.5}$$

The total transmission T can be given by

$$T = \frac{n_4}{n_1} |\frac{1}{B_{2,2}}|^2 \tag{J.6}$$

for normal incident beam.

The overall absorption for the given interface absorption coefficient γ and volume absorption coefficient α can be calculated using

$$A = 1 - R - T. \tag{J.7}$$

References

[1] L. Gallais, P. Voarino, and C. Amra, "Optical measurement of size and complex index of laser-damage precursors : the inverse problem," *J.Opt.Soc.Am.B*, vol. 21, no. 5, pp. 1073–1080, 2004.

[2] A.Alexandrovski, M. Fejer, A. Markosyan, and R. Route, "Photothermal common-path interferometry: new developments," *Proc. of SPIE*, vol. 7193, pp. 1–13, 2009.

[3] W. B. Jackson, N. M. Amer, A. C. Boccara, and D. Fournier, "Photothermal deflection spectroscopy and detection," *APPLIED OPTICS*, vol. 20, no. 8, pp. 1333–1344, 1981.

[4] C. Rodriguez and W. Rudolph, "in preparation,"

[5] A. B. Papandrew, C. J. Stolz, Z. L. Wu, G. E. Loomis, and S. Falabella, "Laser conditioning characterization and damage threshold prediction of Hafnia silica multilayer mirrors by photothermal microscopy," *Annual Symposium on Optical Materials for High Power Lasers*, 2000.

[6] M. Alvisi, M. D. Giulio, S. G. Marrone, M. R. Perrone, M. L. Protopapa, A. Valentini, L. Vasanelli, I. Nazionale, and D. Interateneo, "HfO2 films with high laser damage threshold," *Thin Solid Films*, vol. 358, pp. 250–258, 2000.

[7] K. Choi, J. Meijer, T. Msuzawa, and D. Kim, "Excimer laser micromachining for 3D microstructure," *J.Mater.Process.Technol.*, vol. 149, pp. 561–566, 2004.

[8] C. Fenic, R. Dabu, A. Stratan, C. Blanaru, C. Ungureanu, and C. Luculescu, "Preliminary studies of material surface cleaning with a multi-pulse passively Q-switched Nd:YAG laser," *Opt.Laser Technol*, vol. 36, pp. 125–130, 2004.

[9] A. Bettinger and M. Decroisette, "Laser megajoule project and impact on the inertial fusion program," *Fusion Eng.Design*, vol. 46, pp. 457–460, 1999.

[10] M. Orrit and J. Bernard, "Single pentacene molecules detected by fluorescence excitation in a p-TerphenyI crystal," *Physical Review Letters*, vol. 65, no. 21, pp. 2716–2719, 1990.

[11] S. Berciaud, D. Lasne, G. A. Blab, L. Cognet, and B. Lounis, "Photothermal heterodyne imaging of individual metallic nanoparticles : Theory versus experiment," *Physical Review B*, pp. 1–8, 2006.

[12] B. Bertussi, J.-Y. Natoli, and M. Commandré, "High-resolution photothermal microscope : a sensitive tool for the detection of isolated absorbing defects in optical coatings," *APPLIED OPTICS*, vol. 45, pp. 1410–1415, 2006.

[13] R. Tench, R. Chow, and M. Kozlowski, "Characterization of defect geometries in multilayer optical coatings," *J.Vac.Sci.Technol.A*, vol. 12, pp. 2808–2813, 1994.

[14] M. R. Kozlowski, R. J. Tench, R. Chow, and L. M. Sheehan, "Influence of defect shape on laser-induced damage in multilayer coatings," *Optical Interference Coatings*, vol. 2253, pp. 743–750, 1994.

[15] M. Poulingue, J. DiJon, B. Rafin, H. Leplan, and M. Ignat, "Generation of defects with diamond and silica particles inside high-reflection coatings: influence on the laser damage threshold," *Advances in Optical Interference Coatings*, vol. 3738, pp. 325–336, 1999.

[16] N. J. Dovichi, T. G. Nolan, and W. A. Weimer, "Theory for Laser-Induced Photothermal Refraction," *Anal. Chem.*, vol. 56, no. 2, pp. 1700–1704, 1984.

[17] M. Terazima, N. Hirota, S. E. Braslavsky, A. Mandelis, S. E. Bialkowski, G. J. Diebold, R. J. D. Miller, D. Fournier, R. A. Palmer, and A. Tam, "Quantities , terminology , and symbols in photothermal and related spectroscopies (IUPAC Recommendations 2004)," *Pure Appl. Chem.*, vol. 76, no. 6, pp. 1083–1118, 2004.

[18] S. E. Bialkowski and A. Chartier, "Diffraction effects in single- and two-laser photothermal lens spectroscopy," *APPLIED OPTICS*, vol. 36, no. 27, pp. 6711–6721, 1997.

[19] M. Mero, J. Liu, and W. Rudolph, "Scaling laws of femtosecond laser pulse induced breakdown in oxide films," *Physical Review B*, vol. 71, no. 11, 2005.

[20] D. Grosso and P. A. Sermon, "Scandia optical coatings for application at 351 nm," *Thin Solid Films*, vol. 368, pp. 116–124, 2000.

[21] A. Foster, F. Gejo, A. Shluger, and R. Nieminen, "Vacancy and interstitial defects in hafnia," *Phys. Rev. B*, p. 174117, 2002.

[22] N. W. Ashcroft and N. D. Mermin, *Solid State Physics.* Harcourt, 1976.

[23] L. A. Emmert, M. Mero, and W. Rudolph, "Modeling the effect of native and laser-induced states on the dielectric breakdown of wide band gap optical materials by multiple subpicosecond laser pulses," *Journal of Applied Physics*, vol. 108, no. 4, 2010.

[24] "ISO1151:Test Method for absorptance of Optical Laser Components." International Organization for Standardization, Technical Comittee: Optics and Optical Instruments,subcomittee: Lasers and Laser-Related Equipment, International Standard, Geneve,Switzerland, International Organization Standardization., 1997.

[25] H. S. Carslaw and J. C. Jaeger, "Conduction of Heat in Solids, 2nd ed.," *Clarendon, Oxford*, 1959.

[26] J. Xu, M. Zhu, Y. Zhao, and J. Shao, "Photo-thermal tomograph of optical coatings based on surface thermal lensing technology," *Proc. of SPIE*, pp. 819010–1, 2011.

[27] J. D. Ingle, Jr. and S. R. Crouch, *Spectrochemical Analysis.* Prentice Hall, 1988.

[28] J. T. Verdeyen, *Laser Electronics.* Prentice Hall, 1995.

[29] A. J. Schmidt, *Optical Characterization of Thermal Transport from the Nanoscale to the Macroscale.* PhD thesis, Massachusetts Institute of Technology, 2008.

[30] "Laser-Induced Damage in Optical Materials: 40th Anniversary Collected Papers on DVD," *SPIE,Bellingham, WA*, pp. 377–379, 1969-2009.

[31] A. Rosenfeld, M. Lorenz, R. Stoian, and D. Ashkenasi, "Ultrashort-laser-pulse damage threshold of transparent materials and the role of incubation," *Applied Physcis A*, vol. 376, pp. 373–376, 1999.

[32] A. Shluger, M. Georgiev, and N. Itoh, "Self-trapped excitons and interstitial-vacancy pairs in oxides," *Phil.Mag.B*, vol. 63, pp. 955–964, 1991.

[33] M. Mero, A. J. Sabbah, J. Zeller, and W. Rudolph, "Femtosecond dynamics of dielectric films in the pre-ablation regime," *Applied Physcis A*, vol. 324, no. 81, pp. 317–324, 2005.

[34] X. Zhang, L. A. Emmert, and W. Rudolph, "Time-dependent absorption of TiO_2 optical thin films under pulsed and CW 790 nm laser irradiation, accepted requires minor changes," *Applied Optics*, 2013.

[35] M. Commandré and E. Pelletier, "Measurements of absorption losses in TiO_2 films by a collinear photothermal deflection technique," *Appl. Opt.*, vol. 29, pp. 4276–4283, 1990.

[36] Z. Wu, C. Tan, J. Arndt, and Z. Fan, "Relaxatioin of dielectric thin films under Ar^+ laser irradiation," *Proc.of SPIE*, vol. 1848, pp. 224–233, 1992.

[37] Z. Wu, M. Reichling, X. Hu, K. Balasubramanian, and K. H. Guenther, "Absorption and thermal conductivity of oxide thin films measured by photothermal displacement and reflectance methods," *Appl. Opt.*, vol. 32, pp. 5660–5665, 1993.

[38] R. A. Weber, C. Rodriguez, D. N. Nguyen, L. A. Emmert, D. Patel, C. Menoni, and W. Rudolph, "Third harmonic microscopy of intrinsic and induced material anisotropy in dielectric thin films," *Opt. Eng*, vol. 51, 2012.

[39] H. Bercegol, "What is laser conditioning? A review focused on dielectric multilayers," *Laser-Induced Damage in Optical Materials*, 1998.

[40] C. R. Wolfe, M. R. Kozlowski, J. H. Campbell, F. Rainer, A. J. Morgan, and R. P. Gonzales, "Lawer conditioning of optical thin films," *Laser-Induced Damage in Optical Materials*, 1989.

[41] D. N. Nguyen, L. A. Emmert, M. Mero, D. Patel, E. Krous, C. S. Meroni, and W. Rudolph, "The effect of Annealing on the subpicosecond breakdown behavior of Hafnia films," *Proc.of SPIE 7132*, p. 71320N, 2008.

[42] J.-Y. Natoli, L. Gallais, H. Akhouayri, and C. Amra, "Laser-induced damage of materials in bulk, thin film, and liquid forms," *Appl. Opt.*, pp. 3156–3166, 2002.

[43] *Handbook Optical Constants.* ed Palik.

[44] S. J. Sheldon, L. V. Knight, and J. M. Thorne, "Laser-induced thermal lens effect : a new theoretical model," *Appl.Opt.*, vol. 21, no. 9, pp. 1663–1669, 1982.

[45] M. V. Klein and T. E. Furtak, *Optics.* John Wiley & Sons, Inc., 1986.